Materials Today Communications 52 (2026) 115016

Contents lists available at ScienceDirect

Materials Today Communications

journal homepage: www.elsevier.com/locate/mtcomm

Enhanced corrosion protection of bio-inspired textured AA2024 via optimized plasma electrolytic oxidation coatings

Andrea Cristoforetti [a,*], Matteo Gamba [b], Andrea Brenna [b], Marco Ormellese [b], Michele Fedel [a]

[a] Department of Industrial Engineering, University of Trento, Trento, TN 38123, Italy
[b] Department of Chemistry, Materials and Chemical Engineering "Giulio Natta", Politecnico di Milano, Via Mancinelli 7, Milan 20131, Italy

ARTICLE INFO

Keywords:
Plasma electrolytic oxidation
AA2024 aluminum alloy
Layered double hydroxides
Biomimetic surface texturing
Corrosion protection

ABSTRACT

This study investigates the corrosion resistance and durability of Plasma Electrolytic Oxidation (PEO) coatings on flat and biomimetic-textured (riblet) AA2024 aluminum alloy substrates. Two silicate-based electrolytes were compared: a reference alkaline bath and a modified formulation containing 10 g/L of acetic acid designed to regulate plasma discharge kinetics. To further enhance barrier properties, a hydrothermal post-treatment sealing ZnAl-based was applied. Morphological analysis showed that the addition of acetic acid reduced the average coating thickness from 19 ± 1 μm to 14 ± 1 μm while promoting a significantly denser oxide structure. Electrochemical Impedance Spectroscopy in freshwater revealed that the sealed hybrid system achieved a low-frequency impedance modulus ($|Z|_{0.01\ Hz}$) of $2.9{\cdot}10^7$ Ω·cm² on flat substrates and $1.7{\cdot}10^6$ Ω·cm² on textured riblets, representing an increase of up to three orders of magnitude compared to the bare alloy (10^3 Ω·cm²). Potentiodynamic polarization corroborated these findings, demonstrating that the sealed systems achieve corrosion current densities two orders of magnitude lower than the untreated alloy in simulated freshwater. In aggressive simulated seawater, while the higher chloride concentration triggers a general increase in current density, the sealed coatings maintain a significant performance advantage, outperforming unsealed PEO formulations by at least one order of magnitude. Accelerated corrosion testing confirmed exceptional durability, with the hybrid coatings remaining intact after 2000 h of continuous Neutral Salt Spray exposure. Conversely, cyclic Prohesion testing triggered localized failure after approximately 500 h, highlighting the role of salt crystallization in promoting coating perforation. These results validate the hybrid PEO-LDH system as a robust protection strategy that preserves the integrity of functional surface textures for aeronautical and marine applications.

1. Introduction

Aluminum alloy AA2024 is extensively employed in the aerospace and transport industries due to its high specific strength, fatigue resistance, and good machinability, making it suitable for structural components operating under demanding service conditions [1]. Nevertheless, its microstructural heterogeneity, particularly the presence of Cu-rich intermetallic particles, renders it highly susceptible to localized corrosion in chloride-containing environments [2,3]. These intermetallics act as local cathodes, promoting pitting initiation and intergranular corrosion that severely affect the alloy's durability [4,5].

Several alternative surface treatments have been developed to improve the corrosion resistance of aluminium alloys. Conventional sulfuric acid anodizing and hard anodizing are widely adopted in aerospace applications due to their industrial scalability and ability to produce relatively thick oxide layers [6]. However, these coatings are typically amorphous, mechanically softer, and may require additional sealing to ensure long-term corrosion resistance. Conversion coatings, including chromium-free systems, provide good initial protection but generally form thin layers with limited wear resistance and reduced durability in aggressive chloride environments [7]. Sol-gel coatings enable the formation of dense hybrid organic–inorganic films with tailored functionalities, though their mechanical robustness and adhesion under cyclic environmental exposure may be limited [8]. Thermal spray and other high-temperature deposition techniques can generate thick protective layers, but they often involve higher processing

* Corresponding author.
E-mail addresses: andrea.cristoforetti@unitn.it (A. Cristoforetti), matteo.gamba@polimi.it (M. Gamba), andrea.brenna@polimi.it (A. Brenna), marco.ormellese@polimi.it (M. Ormellese), michele.fedel@unitn.it (M. Fedel).

https://doi.org/10.1016/j.mtcomm.2026.115016
Received 5 January 2026; Received in revised form 2 March 2026; Accepted 17 March 2026
Available online 18 March 2026

complexity and may not ensure conformal coverage over intricate microstructured geometries [9]. Furthermore, conventional organic painting systems were not considered suitable for this specific application, as the high thickness and inherent levelling behaviour of polymer resins would fill the riblet grooves, effectively neutralizing the aerodynamic benefits of the biomimetic texturing.

In this context, Plasma Electrolytic Oxidation (PEO) offers distinct advantages, including the formation of thick, crystalline, strongly adherent oxide layers directly grown from the substrate through plasma-assisted anodization [10,11]. Compared to conventional anodizing, PEO coatings exhibit improved hardness, higher thermal stability, and enhanced wear resistance. Moreover, the process enables better integration with post-treatments such as sealing, facilitating the development of multifunctional hybrid systems [12]. These features make PEO particularly attractive for applications involving complex surface morphologies, such as biomimetic riblet textures, where coating uniformity and durability are critical.

From a quantitative standpoint, conventional anodizing on AA2024 generally produces oxide layers in the order of a few to tens of micrometres, whereas sol-gel and conversion coatings are typically limited to sub-micrometric or few-micrometre thicknesses. While these systems can provide adequate short-term corrosion protection, their polarization resistance in chloride-containing environments often remains lower than that reported for optimized PEO coatings. PEO, instead, enables the growth of thicker and partially crystalline oxides, frequently exceeding 10 μm, with significantly enhanced barrier properties, especially when combined with post-sealing treatments. However, the intense discharge activity intrinsic to the process leads to surface porosity and microcracks, which may compromise long-term protection. These defects result from localized high-temperature plasma events that generate gas evolution and rapid solidification, producing a heterogeneous oxide with open pores and weakly compacted regions [13]. Tailoring the electrolyte composition, by introducing additives such as acetic acid or silicates, has proven effective in stabilizing plasma discharges, reducing defect density, and enhancing coating compactness [11]. Organic acids like acetic acid at the alkaline pH typical of PEO electrolytes are usually fully deprotonated. In this form, they are able to adhere to the substrate surface, thus thickening the overall dielectric layer and moderating discharge intensity. In this way, the growth of finer, more uniform oxides is promoted [14]. This effect has been shown with different kinds of organic acids, even though acetic acid proved to offer a better discharge intensity reduction due to its smaller organic chain length [15]. Unlike bulkier organic complexing agents (e.g., phytates) or other inorganic additives (e.g., aluminates), acetic acid was specifically selected for its short molecular chain and high mobility in the deprotonated state; these features facilitate rapid adsorption at the breakdown sites, effectively mitigating discharge intensity while maintaining a lower electrolyte complexity. Silicate species, instead, contribute to the in-situ incorporation of SiO_2, improving layer adhesion and dielectric integrity [13,16].

Recent research has also focused on coupling corrosion protection with functional surface texturing. Bio-inspired riblet geometries, mimicking shark-skin denticles, can reduce aerodynamic drag and improve energy efficiency in aerospace and marine applications [3,17,18]. The Through-Mask Electrochemical Micromachining (TMEMM) technique offers a precise and scalable approach to producing such biomimetic patterns directly on metallic surfaces [19]. Yet, achieving uniform PEO coatings on these complex morphologies remains challenging due to non-uniform electric fields and localized discharge intensity, which cause heterogeneous oxide growth and localized defects [10].

To overcome these limitations, post-treatment with ZnAl-based Layered Double Hydroxides (LDH) has been proposed to seal residual porosity and impart self-healing capabilities through anion-exchange mechanisms [12,20]. Combining PEO with LDH sealing yields hybrid coating systems exhibiting improved barrier properties and enhanced electrochemical stability [21]. LDHs are lamellar compounds characterized by positively charged brucite-like layers and interlayer anions that can be exchanged or replaced in response to environmental stimuli. When formed on aluminium substrates, ZnAl–LDHs provide both a physical sealing effect, by partially converting the outer Al_2O_3 layer into a dense, ion-impermeable structure, and a chemical self-healing capability through anion-exchange processes that capture aggressive species such as Cl^- while releasing inhibitive ones [22]. Several studies have demonstrated that hydrothermal conversion of the PEO oxide in $Zn(NO_3)_2$-based solutions promotes the formation of a continuous LDH layer, improving ionic resistivity and stabilizing the oxide, electrolyte interface [23]. Mohedano et al. [20] reported that the in-situ growth of ZnAl–LDH on PEO-coated AA2024 significantly reduced chloride ingress and extended the time to corrosion initiation. Similarly, Liu et al. [21] showed that post-sealing treatments based on ZnAl–LDH formation effectively enhanced barrier properties and mitigated localized attack by hindering oxygen and ion transport through the oxide layer. Several other studies confirmed the improvement of the overall corrosion resistance of the coating [24–26].

In this context, the present study investigates the corrosion behavior and durability of PEO coatings applied to both flat and biomimetic-textured AA2024 substrates fabricated via TMEMM. The influence of electrolyte modification with acetic acid and subsequent ZnAl–LDH sealing on coating compactness, microstructural integrity, and corrosion resistance was systematically assessed. The addition of acetic acid to the silicate-based electrolyte was intended to modulate plasma discharge characteristics, suppress high-energy breakdown events, and promote the growth of a finer and denser oxide. The subsequent LDH post-treatment was designed to seal residual porosity and introduce a lamellar barrier layer with enhanced ionic resistivity, contributing to improved long-term electrochemical stability. This work addresses the critical technological hurdle of protecting complex micro-geometries without neutralizing their aerodynamic benefits. Unlike conventional studies focused on flat substrates, we present an original investigation into the synthesis and durability of PEO coatings directly applied to biomimetic-textured AA2024 alloy. The research provides an unprecedented quantitative comparison of corrosion performance between textured and planar coated surfaces, demonstrating that optimized potential-controlled regimes can achieve superior environmental protection while strictly preserving the functional riblet profile.

Electrochemical impedance spectroscopy (EIS), potentiodynamic polarization (PDP), and accelerated corrosion tests (ASTM B117 [27] and ASTM G85 [28]) were employed to quantify the protective performance under both freshwater and seawater conditions. Beyond evaluating corrosion protection, the study aims to elucidate the coupled effects of surface topography and plasma dynamics during oxide growth on microstructured substrates. The integration of TMEMM texturing with optimized PEO and LDH treatments enables a systematic examination of how curvature-induced electric field gradients influence discharge localization, coating uniformity, and sealing efficiency.

The findings provide fundamental insight into the interplay between microtextured geometries, plasma discharge behavior, and oxide formation kinetics, establishing processing, structure, and property relationships relevant for the design of multifunctional aluminum surfaces. The proposed approach offers a scalable route to fabricate engineered surfaces that combine aerodynamic or hydrodynamic efficiency with long-term environmental durability, advancing the applicability of hybrid PEO-LDH systems for aerospace and marine applications. From an application perspective, it is important to clarify that the present approach is not intended for the treatment of entire airframes or ship hulls, but rather for selective functional areas where surface texturing provides measurable aerodynamic or hydrodynamic benefits. Bio-inspired riblet structures are typically implemented on specific and localized regions such as control surfaces, flap systems, leading edges, or marine appendages, where the characteristic treated surface area may range from decimetre-scale panels to about one square meter per component. These dimensions are compatible with currently

available industrial PEO installations, which have already been implemented for medium-sized aerospace and automotive components. Therefore, while full-scale structural upscaling of PEO remains technically demanding due to energy input and power supply constraints, the selective application of hybrid PEO–LDH systems on functionalized regions represents a realistic and scalable scenario.

2. Materials and methods

2.1. Sample production

The substrates used in this study were AA2024-T3 aluminum alloy (Q-LAB, USA; 3.8–4.2 wt% Cu, 1.2–1.8 wt% Mg, 0.3–0.9 wt% Mn) with an exposed surface area of 3 cm^2. Two types of specimens were considered: flat and biomimetic-textured surfaces. The latter were fabricated using TMEMM technique to reproduce shark-skin-inspired riblets optimized in a previous work [17]. PEO treatments were carried out in a 0.5 L cell endowed with a Ti-MMO cathode mesh. A programmable power supply Asterion 751 (California Instruments, USA), was employed to apply a pulsed bipolar signal. All treatments were carried out under potentiostatic control using a stepwise voltage program consisting of successive anodizing stages with increasing applied potentials (4 steps, see Appendix Fig. A.1). Each stage included a voltage ramp followed by a holding plateau, allowing progressive thickening of the oxide layer. The total treatment duration was approximately 15 min. Based on literature data for alkaline silicate electrolytes, dielectric breakdown of aluminium typically occurs above ~300 V (V_{rms}). Accordingly, the first anodizing step was set close to this threshold in order to promote controlled initiation of plasma micro-discharges. Subsequent voltage increments were applied to sustain the discharge regime while avoiding excessive localized overheating, reaching a maximum anodic potential of 454 V. Between consecutive steps, an adequate pause was introduced to allow the electrolyte temperature to return to the controlled value (5 °C), thus ensuring stable and reproducible plasma conditions. During processing, current and voltage signals were continuously recorded to monitor the evolution of the discharge behaviour (as in Fig. 1). The initial stage corresponds to barrier-type anodic oxide formation, followed by dielectric breakdown and the onset of localized plasma micro-discharges. In the steady-state regime, coating growth results from the dynamic balance between oxide formation at the metal/oxide interface and plasma-assisted melting and re-solidification at discharge sites. The primary anodic reaction governing oxide formation can be described as:

$$2Al + 3H_2O \rightarrow Al_2O_3 + 6H^+ + 6e^- \quad (1)$$

Under dielectric breakdown conditions, localized high-temperature plasma events promote partial melting and phase transformation of alumina, along with incorporation of silicate species from the electrolyte into the growing oxide. These processes lead to the formation of a duplex coating structure consisting of a relatively compact inner barrier layer and a more porous outer layer generated by discharge channels. The selected waveform, widely reported in literature for optimized PEO processing [29–31], consisted of 60% anodic and 40% cathodic polarization within each cycle, with a cathodic peak equal to 7% of the anodic one and no off-time (100% duty cycle) (Appendix Fig. A.1). This configuration enabled stable plasma discharges during anodic polarization and efficient oxide growth. The base oxidation bath consisted of hydroxides, silicates, and glycerine. Glycerine, despite not being involved in plasma reactions, is able to retard the electrolyte boiling and splashing out, in order to reduce the plasma aggressiveness, resulting in a less porous and defected coating [32,33]. Samples treated in this reference electrolyte are hereafter denoted as KNS, where the acronym refers to the main alkaline and inorganic components (KOH, NaOH, and Silicate). In the modified electrolyte, 10 g L^{-1} of acetic acid was added to modulate plasma discharge behaviour; these samples are denoted as KNSA, signifying the addition of acetic acid to the base formulation. Post-treatment involved a hydrothermal sealing step for selected coatings, in which the as-formed alumina layer was partially converted into ZnAl-LDH. This process was carried out by immersing the PEO-coated samples for 15 min in a 0.05 mol L^{-1} $Zn(NO_3)_2{\cdot}6H_2O$ aqueous solution maintained at 90 °C and pH 6.5. All the parameters were optimized in a previous study [34]. After sealing, all specimens were rinsed with deionized water and air-dried prior to characterization and corrosion testing. The main process parameters and electrolyte compositions are summarized in Table 1. All chemical reagents used throughout the experimental campaign were of analytical grade and were purchased from Sigma-Aldrich (Merck KGaA, Darmstadt, Germany).

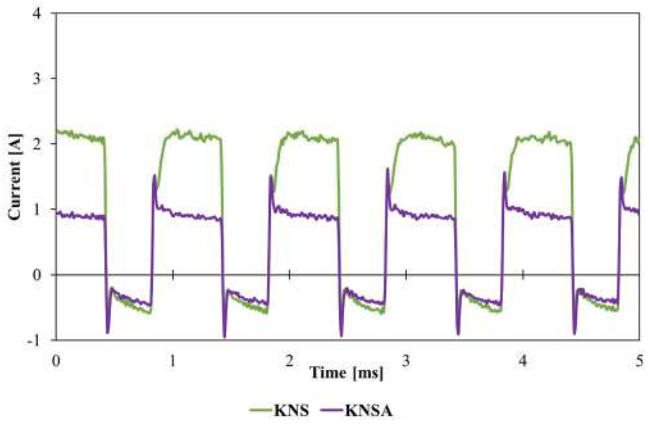

Fig. 1. Current acquisitions during PEO measured at 330 V_{rms}, 10 s before the end of the anodizing step n.3.

2.2. Characterization

Characterization of the coatings involved Scanning Electron Microscopy (SEM) (Jeol JSM-IT300, Japan) for morphological analysis, especially to investigate coating defects and degradation features after testing. X-ray diffraction (XRD) patterns were obtained on the coated samples using a Philips PW3020 goniometer (Milan, Italy) with Cu Kα1 radiation (1.54058 Å). Acquisition angle ranged from 5.01° to 69.96° with 0.03° steps. Electrochemical measurements were performed in a conventional three-electrode glass cell with a total volume of 500 mL. The exposed AA2024 working electrode area was 3 cm^2. A platinum mesh served as counter electrode, while an Ag/AgCl reference electrode (in saturated KCl solution, +0.196 V vs SHE at 25 °C (Mettler Toledo, Switzerland)) was used for potential control using a Metrohm Autolab potentiostat PGSTAT (Metrohm, Netherlands). All reported potentials are referred to the Ag/AgCl reference electrode unless otherwise specified.

PDP tests were conducted by scanning the potential from −300 mV to + 300 mV versus open circuit potential with a potential scan rate of 10 mV/min, according to ASTM G61 standard. EIS was performed using a 10 mV RMS sinusoidal excitation over a frequency range from 10^5 Hz to 10^{-2} Hz. Tests were conducted in electrolytes simulating freshwater (20 ppm Cl^-) and seawater (20,000 ppm Cl^-). Measurements were normalized to the actual exposed surface area, considering the surface roughness factor of textured samples (~1.9).

EIS measurements were performed on as-prepared samples to provide an initial diagnostic ranking of the coatings' barrier properties and intrinsic defectiveness. Long-term immersion monitoring was intentionally excluded as the study prioritized atmospheric and cyclic corrosion resistance (cabinet tests), which involve degradation mechanisms and oxygen diffusion kinetics that do not directly correlate with stagnant bulk immersion conditions, consistent with the lack of established correlations in the literature for PEO systems on aeronautical alloys.

Table 1
PEO process electrolytes composition, sealing step, and coating thickness.

sample	OH^- [mol/L]	KOH [mol/L]	NaOH [mol/L]	CH_3COOH [g/L]	Na_2SiO_3 [g/L]	Glycerin [g/L]	Sealing ZnAl-LDH	Thickness [μm]
KNS	0.09	0.014	0.076	-	10	10	-	19 ± 1
KNS+LDH	0.09	0.014	0.076	-	10	10	90°C 15 min	19 ± 1
KNSA	0.09	0.014	0.076	10	10	10	-	14 ± 1
KNSA+LDH	0.09	0.014	0.076	10	10	10	90°C 15 min	14 ± 1

2.3. Accelerated aging

Accelerated corrosion tests included ASTM B117 [27] neutral salt spray (NSST) and Prohesion test or ASTM G85 dilute electrolyte cyclic fog/dry test [28] (Ascot Analytical, UK). The salt spray test exposed samples to continuous atomized 5 wt% NaCl fog at 35 ± 2 °C for up to 2000 h, to assess chloride-induced corrosion under highly aggressive conditions. The Prohesion test subjected samples to cyclic wet and dry periods with alternate exposure to a mist of 0.05 wt% NaCl and 0.35 wt % NH_4HSO_4 at ambient temperature followed by dry-off at 35 ± 2 °C. This simulates more realistic outdoor atmospheric conditions. The progression of corrosion damage was monitored by optical imaging and SEM.

3. Results

3.1. Coating morphology

The morphological analysis of PEO coatings on both flat and biomimetically textured AA2024 substrates reveals significant differences in coating uniformity, thickness, and fidelity to the underlying surface geometry. An example of the optical appearance of the textured and coated surface is reported in Fig. 2 for the KNS top view and cross-section. The KNS and KNSA coatings exhibit average thicknesses of 18.89 ± 0.77 μm and 13.92 ± 1.01 μm, respectively, with the latter showing reduced growth due to acetic acid's inhibitory effect on plasma discharge initiation. Surface morphology, assessed via SEM, indicates that both coatings display fine, uniformly distributed micro-pores, with KNSA presenting a denser structure and increased micro-corrugations attributed to acetic acid adsorption, which enhances dielectric strength and delays sparking (inset of Fig. 3). The addition of LDH sealing (KNS+LDH and KNSA+LDH) results in partial pore coverage, with lamellar LDH structures observed at higher magnifications (Fig. 4), confirming successful hydrothermal conversion of surface Al_2O_3 into ZnAl-LDH, although the 15-minute treatment limits full pore closure. Cross-section SEM images of the flat PEO-coated samples are reported in Appendix Fig. A.2 as a baseline for comparison. A detailed SEM characterization of the textured surfaces, which constitute the primary focus of this investigation, is instead presented in Fig. 3 to highlight the influence of riblet geometry on coating uniformity and fidelity. Regarding the riblet peaks observed in Fig. 3, minor variations in geometry, ranging from slightly flattened to more acicular profiles, can be observed

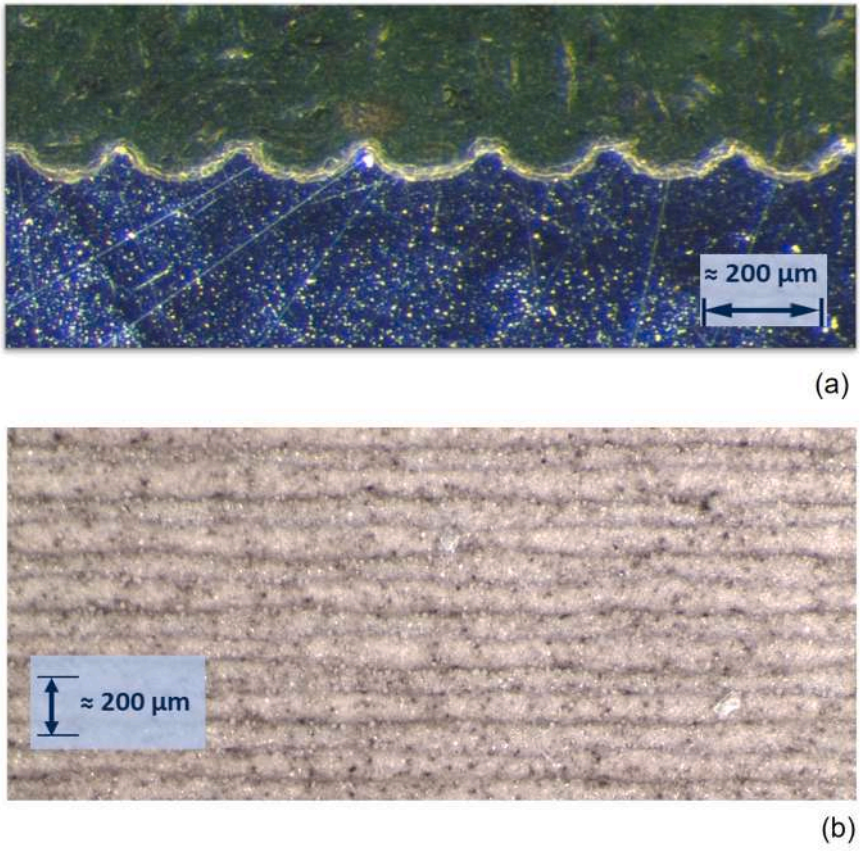

Fig. 2. Optical micrographs of the biomimetic-textured aluminium alloy AA2024 coated with Plasma Electrolytic Oxidation (PEO) in the silicate-based reference electrolyte (KNS). (a) Cross-sectional view showing the fidelity of the oxide layer to the riblet geometry; (b) Top-view showing the longitudinal arrangement of the textured surface. Scale bars represent approximately 200 μm.

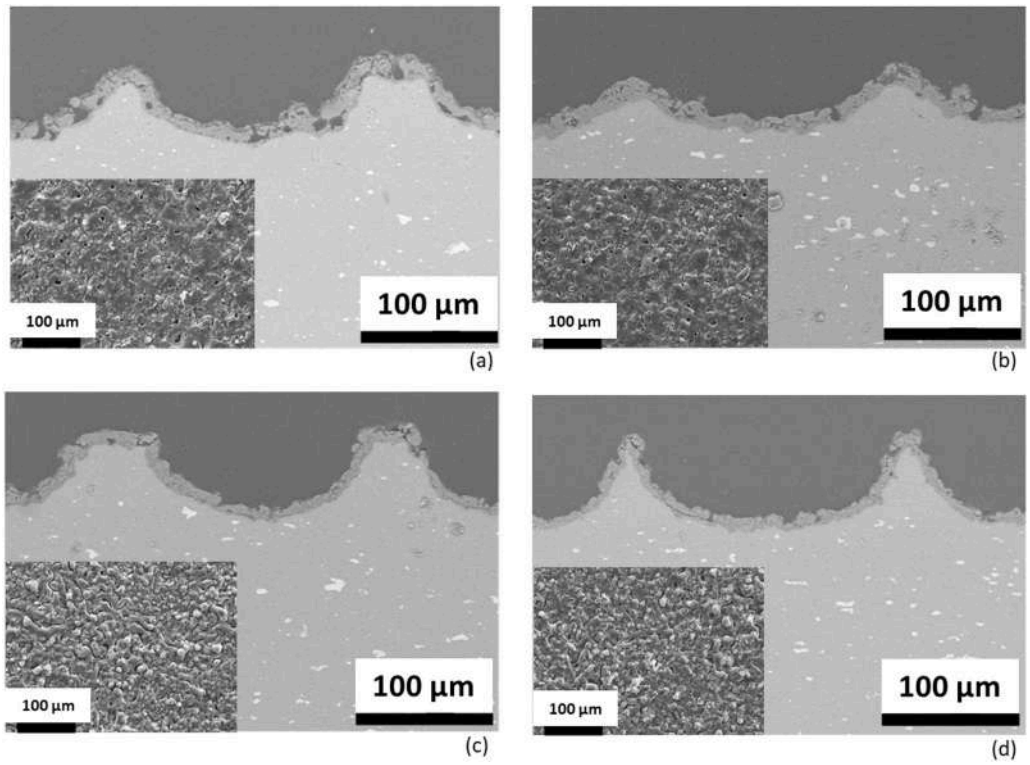

Fig. 3. Scanning Electron Microscopy (SEM) micrographs showing the cross-sectional morphology and surface appearance (insets) of textured AA2024 substrates coated with different Plasma Electrolytic Oxidation (PEO) systems: (a) reference silicate-based coating (KNS); (b) reference coating sealed with ZnAl Layered Double Hydroxides (KNS+LDH); (c) coating produced with the addition of acetic acid (KNSA); (d) acetic-acid-modified coating sealed with Layered Double Hydroxides (KNSA+LDH). The images highlight the coating thickness and the preservation of the riblet peaks.

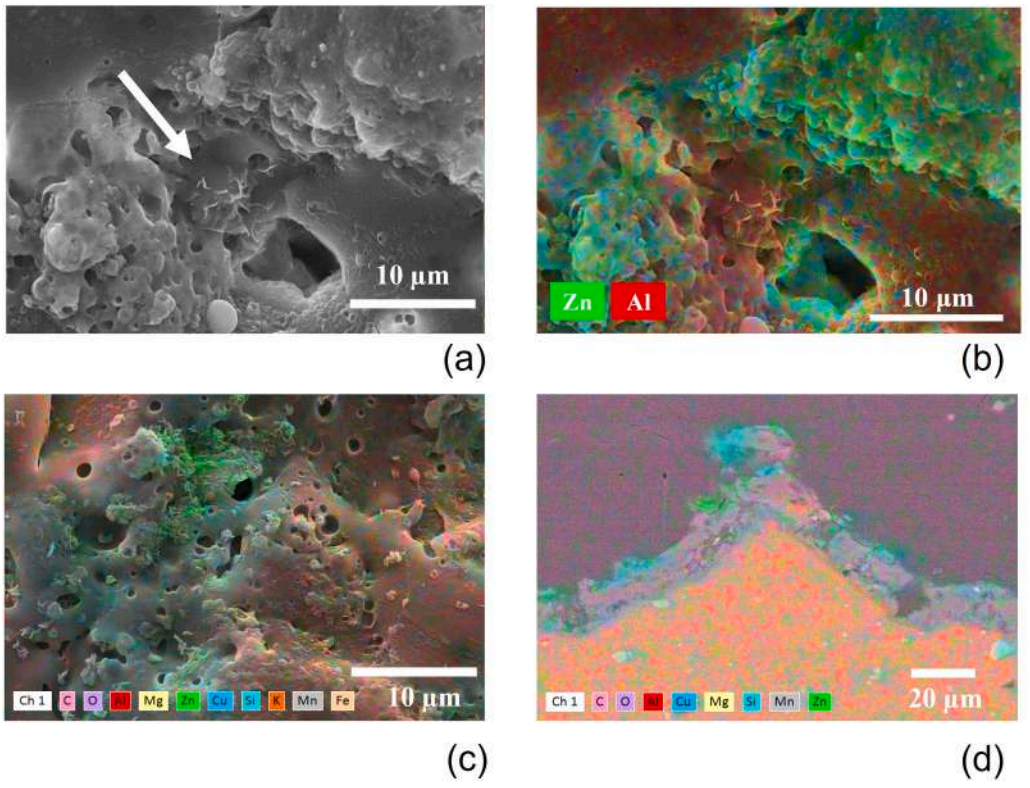

Fig. 4. Detailed Scanning Electron Microscopy (SEM) and Energy Dispersive X-ray Spectroscopy (EDXS) analysis of the KNS+LDH hybrid system. (a) High-magnification surface view showing the lamellar structure of the Layered Double Hydroxides (LDH) clogging the oxide pores (white arrow); (b, c) Elemental maps of Zinc (Zn) and Aluminium (Al) showing the distribution of the sealing phase; (d) EDXS elemental map of the cross-section.

among the different samples. These discrepancies are primarily attributed to the inherent fabrication tolerances of the TMEMM process used for substrate preparation, rather than the subsequent PEO treatment. Crucially, the PEO layer demonstrates high morphological fidelity, consistently following the underlying substrate profile and effectively preserving the functional features of the biomimetic texture regardless of these minor initial geometric variations.

Cross-sectional SEM analysis shows that all coatings conform well to the substrate. Furthermore, the coatings elemental composition has been confirmed to be similarly constituted (EDXS cross-sectional maps in Appendix Fig. A.3). The riblet geometry introduces local curvature variations that are expected to affect electric field distribution during PEO processing. Convex regions (riblet peaks) theoretically experience higher field intensity than valleys, potentially promoting locally intensified discharge events. In the present work, this interpretation is based on established electrostatic considerations combined with morphological and electrochemical observations, rather than on direct spatially resolved measurements. SEM analysis indicates slightly higher surface-connected porosity and defect density in textured samples compared to flat substrates. However, no region-specific quantitative mapping (peak vs. sidewall vs. valley) was performed. A detailed spatially resolved microstructural analysis would provide further insight and represent a valuable direction for future work. Nevertheless, both KNS and KNSA coatings faithfully reproduce the riblet structure, maintaining the designed pitch (~200 μm) and depth (~75–100 μm) with minimal tip rounding, confirming their suitability for aerodynamic applications where drag reduction is critical. Overall, the combination of low-energy PEO parameters and LDH sealing yields coatings with optimal thickness control, reduced porosity, and high morphological fidelity to the biomimetic substrate, balancing corrosion protection with functional surface integrity. The surface homogeneity and porosity of the developed coatings were quantitatively assessed via digital image analysis using ImageJ software on high-resolution SEM top-view micrographs, with the resulting data summarized in Table 2. The reference KNS coating is characterized by a surface porosity area fraction of 4.48% and a mean pore area of 1.74 μm^2, whereas the addition of 10 g/L acetic acid facilitates a notable structural refinement. Specifically, the unsealed KNSA coatings exhibit a reduced surface porosity area fraction of 2.73% and a significantly smaller mean pore area of 1.14 μm^2, confirming that the moderation of plasma discharge energy promotes the formation of a higher density of finer, better-distributed micro-pores rather than large, localized discharge channels. Upon the application of the hydrothermal post-treatment, the LDH layer further seals the residual porosity, leading to a surface porosity area fraction of 1.87% for the KNS+LDH system and 1.65% for the KNSA+LDH one, with a corresponding reduction in the mean pore area to 1.06 μm^2 and 1.08 μm^2, respectively.

The phase composition and crystallinity of the PEO coatings were evaluated via XRD to determine the structural impact of the electrolyte modification (Fig. 5). The diffractograms of the reference KNS coating exhibit a characteristic broad halo between 20° and 35° (2θ), indicative of a predominantly amorphous alumina matrix, alongside reflections corresponding to the cubic γ-Al_2O_3 phase and the underlying AA2024 substrate [33]. Upon the addition of 10 g/L of acetic acid (KNSA), the fundamental phase assembly remains consistent; however, a discernible shift in the amorphous-to-crystalline ratio is observed. The KNSA coatings show a relative increase in the amorphous background and a broadening of the γ-Al_2O_3 peaks, suggesting a decrease in the overall degree of crystallinity compared to the KNS baseline. This effect is directly attributed to the discharge-modulating role of the acetic acid; by lowering the energy density of individual plasma events and mitigating localized high-temperature spikes, the organic additive hinders the thermal-induced transformation of amorphous alumina into more ordered crystalline structures. Consequently, the higher amorphous content in KNSA coatings correlates with the refined pore distribution and improved structural compactness observed in the SEM characterization, as a more disordered matrix favors the formation of a continuous and less defective barrier layer despite the higher crystallinity of the KNS layer.

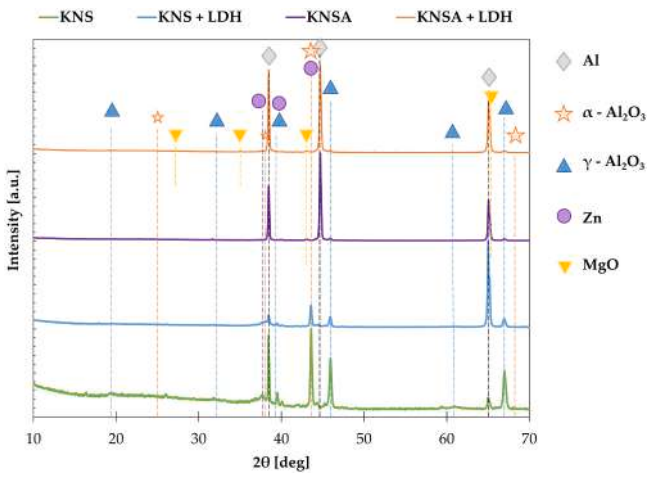

Fig. 5. XRD patterns of PEO coatings produced in the reference silicate electrolyte (KNS) and the acetic-acid-modified formulation (KNSA), together with the sealed coatings.

Table 2
Quantitative evaluation of surface porosity and mean pore area for the unsealed and LDH-sealed PEO coatings produced in the reference (KNS) and acetic-acid-modified (KNSA) electrolytes. These morphological parameters were determined via digital image analysis (ImageJ) of high-resolution SEM micrographs, reflecting the structural refinement and pore-filling efficiency achieved through electrolyte modification and hydrothermal post-treatment.

Sample Type	Average Size (μm^2)	% Pores Area
KNS	1.74	4.48
KNS + LDH	1.06	1.87
KNSA	1.14	2.73
KNSA + LDH	1.08	1.65

3.2. Electrochemical characterization

Electrochemical tests were performed on the four coating systems, KNS, KNS + LDH, KNSA, and KNSA + LDH, both on flat and biomimetic-textured AA2024 substrates. PDP and EIS were conducted in electrolytes simulating freshwater (20 ppm Cl^-) and seawater (20,000 ppm Cl^-). The PDP results confirmed that electrolyte composition and post-treatment significantly influenced the electrochemical performance of the PEO coatings (Fig. 6). The inclusion of acetic acid in the anodizing bath (samples KNSA and KNSA + LDH) led to a marked reduction in coating defectiveness, attributed to the organic additive's ability to modulate plasma discharges and promote a more compact oxide structure [16,31]. Concurrently, a notable decrease in corrosion current density and an anodic shift of the corrosion potential (E_{corr}) were observed, reflecting enhanced barrier performance and a reduction in active dissolution sites.The application of ZnAl LDH sealing further improved the electrochemical stability. The sealed coatings (KNS + LDH and KNSA + LDH) displayed reduced current values in both electrolytes, confirming the beneficial sealing effect on the PEO oxide microstructure. The improvement was particularly pronounced for KNS + LDH, where sealing compensated for the higher porosity of the unsealed base oxide. In contrast, the incremental benefit of sealing was less significant for the acetic-acid-containing coating, which was already compact. In seawater (20,000 ppm Cl^-), all coatings showed a general decrease in protectiveness and more active potentials compared to freshwater, as expected due to the higher chloride concentration. Nevertheless, the performance hierarchy remained consistent: sealed coatings outperformed the

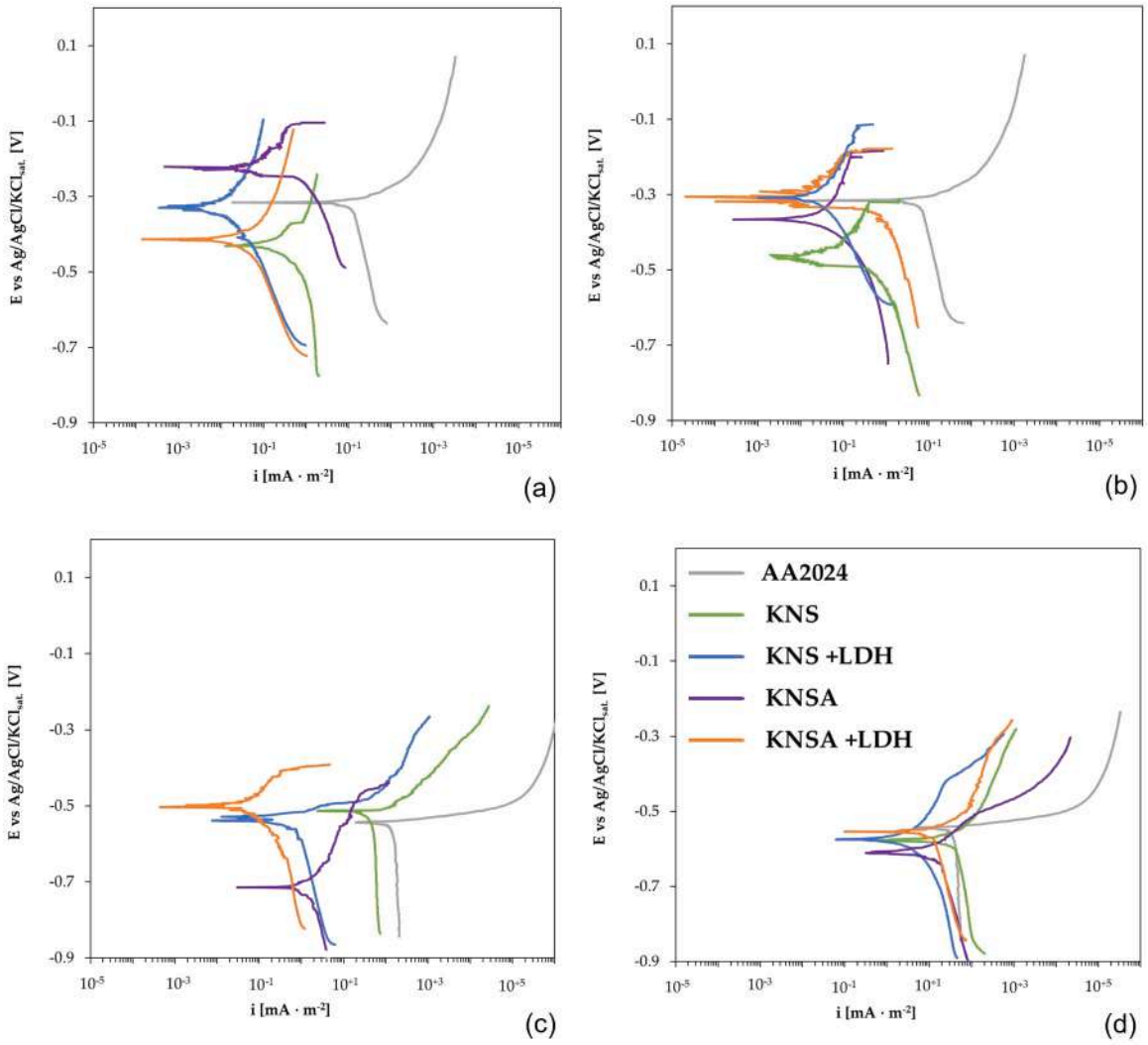

Fig. 6. Potentiodynamic Polarization (PDP) curves for flat and textured PEO-coated AA2024 substrates collected in different chloride-containing environments: (a) flat samples in 20,000 ppm Cl^- (simulated seawater); (b) textured samples in 20,000 ppm Cl^-; (c) flat samples in 20 ppm Cl^- (simulated freshwater); (d) textured samples in 20 ppm Cl^-. The curves illustrate the corrosion current density and the shift in corrosion potential for the different electrolyte formulations and sealing treatments.

unsealed ones, and acetic-acid-modified oxides performed better than their unmodified counterparts. Comparative testing between flat and textured samples revealed that texturing slightly reduced electrochemical performance. On textured surfaces, PEO coatings exhibited higher current ranges, particularly under seawater conditions. This behavior was attributed to increased coating porosity and local field inhomogeneities during PEO growth on corrugated geometries, leading to more intense plasma discharges and uneven oxide formation. Despite this reduction, the sealed coatings retained satisfactory performance, demonstrating the potential of the PEO + LDH approach for protecting functionally textured aluminum surfaces without compromising their aerodynamic functionality. Concerning the EIS in freshwater (Figs. 7a and 7b), the Nyquist plots are characterized by broad and well-defined capacitive semi-circles across all coating systems, reflecting a stable dielectric response and significantly high polarization resistance. The flat KNS + LDH system (Fig. 7a) exhibits the largest capacitive arc, while the textured counterparts (Fig. 7b) display a noticeable contraction of the semi-circles due to the increased porosity and electric field inhomogeneities inherent to the riblet geometry. In general, the EIS spectra in Fig. 7 exhibited multiple time constants associated with the intrinsic porosity of the PEO layer and the presence of structural defects [35]. Furthermore, at the lowest frequencies investigated, the emergence of nonlinearities and non-stationarities prevented the reliable fitting of EIS raw data-sets with an electrical equivalent circuit (EEC). It is likely that the localized electrochemical activity of intermetallic phases induces dynamic surface changes that violate the stationarity and linearity requirements of EIS. Consequently, the resulting non-linearities/non-stationarities at low frequencies preclude a reliable fitting of the raw data sets. Due to the resulting complexity and the challenges in achieving reliable equivalent circuit fitting, a qualitative assessment was performed based on the low-frequency impedance modulus $|Z|_{0.01\ Hz}$ [36,37]. In the low-salinity electrolyte (20 ppm Cl^-), $|Z|_{0.01\ Hz}$ for the flat KNS+LDH system reached approximately $3{\cdot}10^7$ $\Omega{\cdot}cm^2$, while the textured counterpart was recorded at $1.7{\cdot}10^6$ $\Omega{\cdot}cm^2$. This consistent reduction of one order of magnitude for textured specimens aligns with the localized electric field inhomogeneities and increased defect density induced by the riblet geometry. Despite this, all coatings significantly improved the corrosion resistance compared to the bare AA2024 alloy ($|Z|_{0.01\ Hz} = \sim 10^3\ \Omega{\cdot}cm^2$). The unsealed KNS coating proved to be the least protective but derived the most substantial benefit from the post-treatment, with KNS+LDH emerging as the best performer in both test solutions. The inhibitory effect of acetic acid (KNSA) was primarily discernible when comparing unsealed configurations. In simulated seawater (20,000 ppm Cl^-), the performance hierarchy

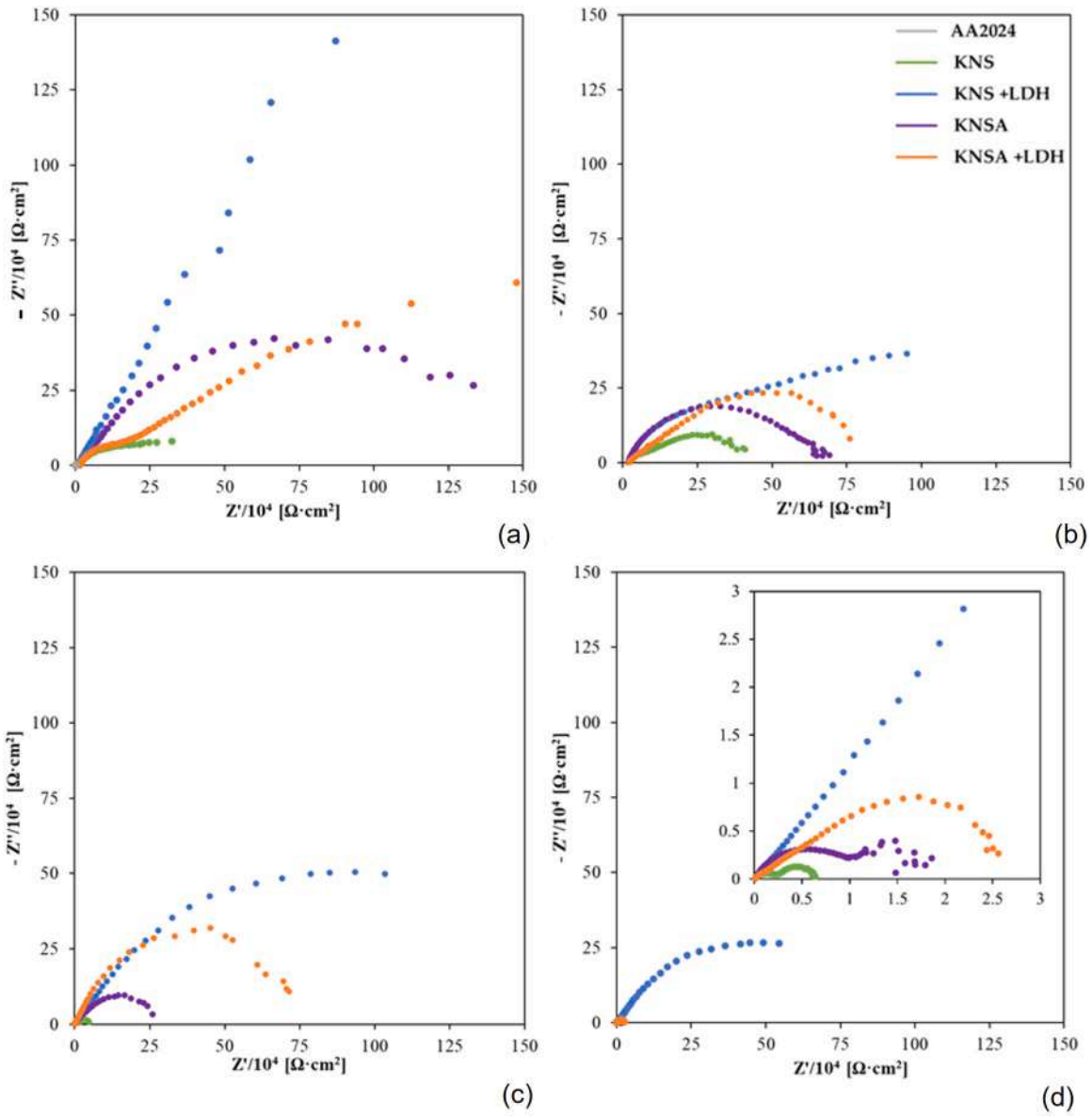

Fig. 7. Electrochemical Impedance Spectroscopy (EIS) Nyquist plots collected after 1 h of immersion in simulated environments: (a) flat samples in 20 ppm Cl^-; (b) textured samples in 20 ppm Cl^-; (c) flat samples in 20,000 ppm Cl^-; (d) textured samples in 20,000 ppm Cl^-. The capacitive arcs represent the dielectric response of the coatings. The inset in (d) provides a detailed view of the lower-impedance systems (KNS and KNSA), which are otherwise compressed by the high impedance of the sealed KNS+LDH system.

remained unchanged. Interestingly, while PDP curves showed attenuated differences due to electrolyte aggressiveness, the EIS data more clearly distinguished the superior barrier properties of the hybrid systems. The specific $|Z|_{0.01\ Hz}$ values for all configurations, together with the corrosion potentials E_{corr}, are reported in the Table 3 and Table 4. Furthermore, a closer inspection of the Nyquist plots in simulated seawater (Figs. 7c and 7d) reveals a distinct change in the corrosion mechanism compared to freshwater. While the unsealed samples (KNS) exhibit a marked contraction of the capacitive arc and a low-frequency tail indicative of diffusion-controlled processes caused by electrolyte penetration into the porous network, the sealed systems, particularly KNS + LDH, retain a predominantly capacitive semi-circle with the highest impedance values. This behaviour suggests that the hybrid barrier effectively hinders chloride migration to the substrate interface, preventing the onset of diffusion-limited attack even under high salinity conditions. Notably, the persistence of the capacitive response in the KNS + LDH and KNSA + LDH coatings confirms that the sealing treatment successfully maintains the dielectric integrity of the oxide,

Table 3
Main electrochemical parameters (E_{corr} and |Z| at 0.01 Hz) obtained from PDP and EIS tests for biomimetically textured AA2024 alloy in freshwater (20 ppm Cl^-) for both unsealed and LDH-sealed PEO coatings.

Sample Type	E_{corr} (Flat) [V vs. Ag/AgCl]	E_{corr} (Textured) [V vs. Ag/AgCl]	|Z| at 0.01 Hz (Flat) [Ω·cm²]	|Z| at 0.01 Hz (Textured) [Ω·cm²]
AA2024	-0.320	-0.317	$4.2{\cdot}10^3$	$4.2{\cdot}10^3$
KNS	-0.430	-0.459	$3.6{\cdot}10^6$	$3.9{\cdot}10^5$
KNS + LDH	-0.329	-0.310	$2.9{\cdot}10^7$	$1.7{\cdot}10^6$
KNSA	-0.221	-0.366	$1.6{\cdot}10^6$	$7.4{\cdot}10^5$
KNSA + LDH	-0.410	-0.310	$1.8{\cdot}10^6$	$8.5{\cdot}10^5$

effectively compensating for the aggressive nature of the chloride-rich environment. This transition is dictated by the chemical interaction of

Table 4
Main electrochemical parameters (E_{corr} and |Z| at 0.01 Hz) obtained from PDP and EIS tests for biomimetically textured AA2024 alloy in simulated seawater (20,000 ppm Cl^-) for both unsealed and LDH-sealed PEO coatings.

Sample Type	E_{corr} (Flat) [V vs. Ag/AgCl]	E_{corr} (Textured) [V vs. Ag/AgCl]	|Z| at 0.01 Hz (Flat) [Ω·cm²]	|Z| at 0.01 Hz (Textured) [Ω·cm²]
AA2024	-0.540	-0.536	$1.1{\cdot}10^3$	$1.1{\cdot}10^3$
KNS	-0.510	-0.580	$4.7{\cdot}10^4$	$1.3{\cdot}10^4$
KNS + LDH	-0.538	-0.575	$2.0{\cdot}10^6$	$5.0{\cdot}10^4$
KNSA	-0.710	-0.610	$2.6{\cdot}10^5$	$2.8{\cdot}10^4$
KNSA + LDH	-0.500	-0.550	$7.1{\cdot}10^5$	$5.0{\cdot}10^5$

chloride ions at the coating/substrate interface once electrolyte penetration through the outer porous layer occurs. The corrosion process is fundamentally governed by the aluminium oxidation of substrate beneath and the oxygen reduction. In high-salinity environments, Cl^- ions promote the breakdown of the inner barrier layer by favouring the formation of soluble aluminium hydroxychlorides, which leads to the transition from a purely capacitive response to a diffusion-controlled regime. However, in sealed systems (KNS + LDH), the LDH layer actively modifies this mechanism by acting as an 'anion trap' [38]. The LDH structure delays the onset of corrosion by capturing chloride ions and releasing non-aggressive species through an anion-exchange process, effectively preserving the dielectric integrity of the oxide even under high chloride concentrations [39]. It should be noted that the EIS analysis was focused on a comparative evaluation of the impedance modulus at the low-frequency limit ($|Z|_{0.01}$ Hz) rather than EEC fitting. This methodological choice is dictated by the high reactivity of the AA2024 substrate in chloride-rich environments; the occurrence of localized activation and non-stationary behaviour, manifested as open circuit potential fluctuations during the scan, potentially compromises the fundamental requirements for reliable quantitative modelling. Therefore, to ensure the scientific integrity of the conclusions, the impedance response was used as a diagnostic tool to rank the barrier properties of the different PEO/LDH systems without introducing the uncertainties inherent in the fitting of non-stationary electrochemical data. In conclusion, it can be affirmed that the coating protectiveness ranking obtained in freshwater is confirmed also for seawater. Although the results are much closer in 20,000 ppm Cl^- than in 20 ppm Cl^- because of the high aggressiveness of the electrolyte, PDP and EIS results confirm that the sealed coatings perform better than the unsealed ones.

3.3. Accelerated aging tests

3.3.1. Neutral salt spray

NSST exposure confirmed the robustness of the PEO coatings, which maintained excellent surface integrity after 2000 h of continuous testing (Fig. 8 and Fig. 9). No significant corrosion products or delamination were detected on either flat or textured specimens. Only minor darkening of localized regions was observed, especially on the textured samples (Fig. 10). SEM–EDXS analyses conducted on these areas revealed no compositional differences between regions of distinct appearance, indicating that the observed color variation does not originate from substrate corrosion or chemical contamination. Instead, this phenomenon is likely related to local oxidation and the rearrangement of amorphous and γ-Al_2O_3 phases into alternative allotropic structures, as also observed by Du et al. [35] during long-term immersion of PEO-coated AA2024. Such structural reorganization may induce local optical contrast without affecting either the chemical composition or the electrochemical stability of the coating. SEM–EDXS analyses conducted on these areas revealed that the constituent elements of the coating remained largely consistent across the surface. However, a closer

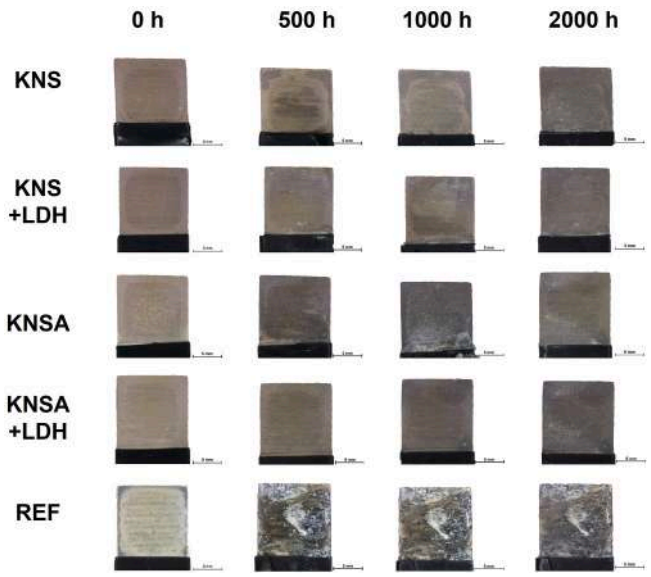

Fig. 8. Evolution of the surface appearance of biomimetic-textured AA2024 samples during 2000 h of Neutral Salt Spray Test (NSST) according to ASTM B117. The figure compares the four PEO-coated systems (KNS, KNS+LDH, KNSA, KNSA+LDH) with an uncoated AA2024 reference (REF) at 0, 500, 1000, and 2000 h, showing the high stability of the treated surfaces.

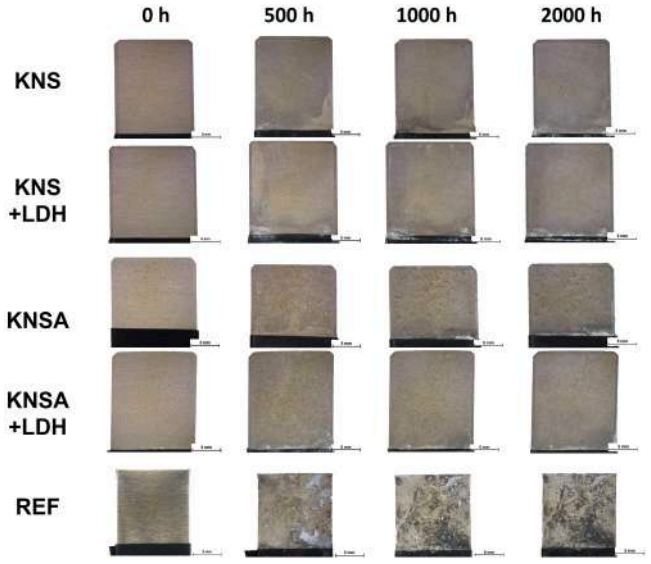

Fig. 9. Evolution of the surface appearance of flat AA2024 samples during 2000 h of Neutral Salt Spray Test (NSST) according to ASTM B117. The images show the integrity of the PEO-coated systems compared to the significant corrosion and pitting observed on the uncoated reference alloy (REF).

inspection of the chlorine map reveals a slight localized enrichment in the darkened regions, which is attributed to the superficial trapping of saline species within the outermost porous layer of the PEO oxide. Crucially, the absence of localized pitting, substrate consumption, or delamination confirms that these chlorides did not penetrate the inner barrier layer or trigger active corrosion processes, even after 2000 h of exposure. This suggests that the observed colour variation arises from a combination of surface interaction with the electrolyte and a possible phase reorganization of the oxide, as further detailed in Appendix Fig. A.4.

To verify the absence of sub-surface or interfacial corrosion, a common phenomenon in PEO-coated aluminum, SEM cross-sections

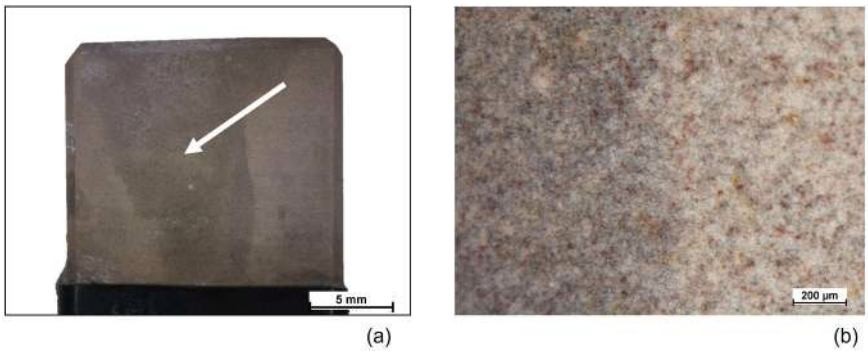

Fig. 10. Detailed investigation of the localized surface darkening observed after 2000 h of salt spray exposure. (a) Macroscopic view of a PEO-coated sample where the white arrow points to a discoloured region; (b) Microscopic optical magnification showing the transition between the darkened and the original area of the coating.

were collected after the full 2000-hour exposure Fig. 11. These analyses confirmed that the barrier integrity was maintained at the microscopic level across all formulations; no evidence of interfacial delamination or substrate attack was detected, demonstrating that the coatings provided a complete and sustained isolation of the substrate from the saline environment.

Despite these superficial color changes, the PEO coatings exhibited remarkable protection compared to the uncoated reference alloy. Both flat and textured samples retained excellent continuity and barrier integrity, confirming the effectiveness of the PEO-LDH hybrid system. The textured specimens displayed a slightly higher frequency of superficial imperfections, likely related to local electric field inhomogeneities during oxide growth, but these remained limited in extent and did not compromise the overall corrosion resistance.

The superior performance observed after 2000 h of NSST exposure aligns with previous reports on PEO coatings containing a compact inner barrier layer and a dense sealing structure. Du et al. [35] demonstrated that optimized plasma regimes producing a thinner outer porous layer and a thicker inner layer maintained protective performances up to 380 h of immersion in 3.5 wt% NaCl solution, with no evidence of interfacial delamination. Similarly, Mohedano et al. [20] reported that ZnAl–LDH post-treatments effectively sealed the open porosity of PEO coatings, improving the stability of the oxide-electrolyte interface under salt fog exposure. In line with these findings, the present results confirm that the combined effect of electrolyte modification and LDH sealing promotes the formation of a highly compact oxide with sustained dielectric behavior and delayed onset of corrosion processes.

The long-term integrity of the PEO-LDH system can be attributed to the synergy between its microstructural compactness and self-sealing properties. The dense inner alumina layer acts as the primary diffusion barrier, while the LDH layer mitigates the ingress of aggressive ions through ion-exchange and physical blockage mechanisms. This

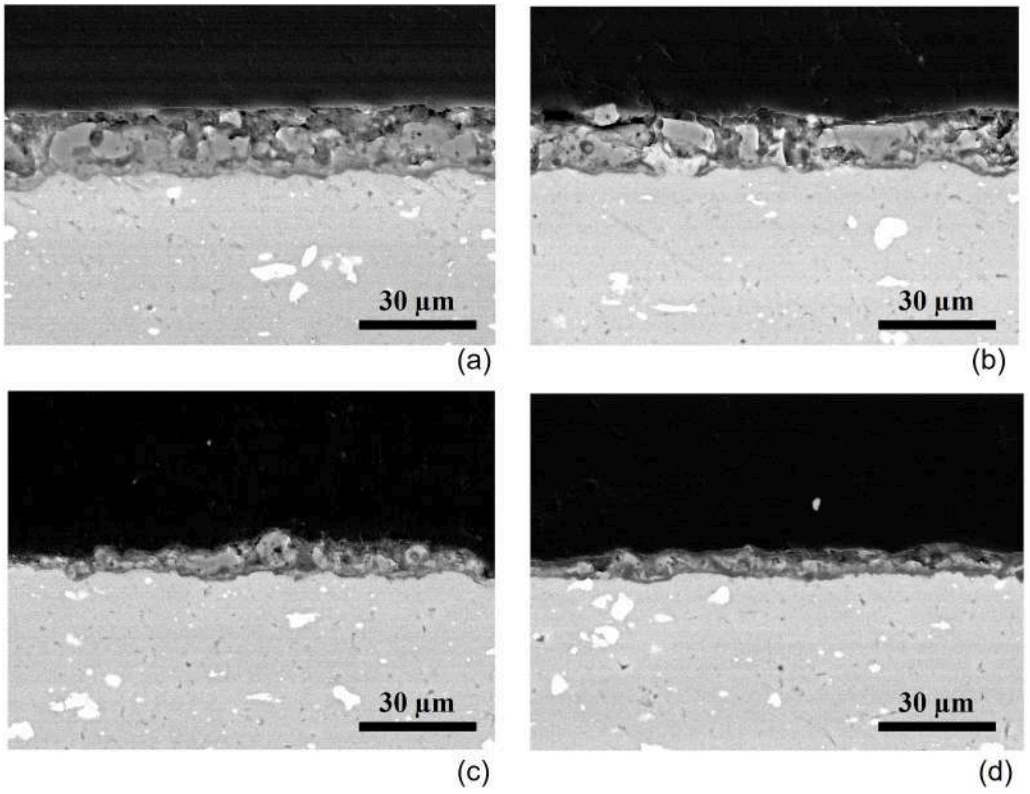

Fig. 11. SEM cross-sections of (a) KNS, (b) KNS+LDH, (c) KNSA, and (d) KNSA+LDH samples after 2000 h of Neutral Salt Spray exposure. The images show a perfectly intact coating-substrate interface across all formulations, confirming the absence of undercoating corrosion.

configuration ensures that corrosion initiation occurs only at extremely late stages, as also inferred from the stable impedance response reported for similarly treated AA2024 alloys [40]. Consequently, the PEO-LDH hybrid system developed in this study provides not only superior passive protection but also enhanced durability under prolonged saline exposure, even in the presence of complex surface geometries.

3.3.2. *Dilute electrolyte cyclic fog/dry test*

The dilute electrolyte cyclic fog/dry test, designed to simulate alternating wet/dry atmospheric exposure, proved markedly more aggressive than the continuous salt spray environment. The first evidence of degradation appeared after approximately 500 h, with white corrosion products forming at localized sites on all coatings (Fig. 12 and Fig. 13). The cyclic crystallization and dissolution of chlorides during drying stages promoted the formation of crater-like defects within the oxide layer, as confirmed by SEM observations Fig. 14. Under cyclic exposure, no appreciable differences were detected among the various coating formulations. The cyclic wet/dry conditions proved extremely aggressive for this type of oxide layer, promoting similar degradation patterns across all samples and making it difficult to discern the subtle performance differences previously observed through electrochemical characterization. This enhanced aggressiveness, despite the lower chloride concentration of the electrolyte, may be attributed to the local build-up of high chloride concentrations caused by evaporation during the dry phases. The repeated crystallization and dissolution of salts likely intensifies local stresses within the coating and accelerates degradation processes. As observed in the salt spray test, the textured specimens showed a slightly higher frequency and size of localized corrosion spots than the flat ones. These defects are attributed to the intrinsic electric field inhomogeneities generated during PEO on corrugated geometries, leading to local variations in coating compactness. Cross-sectional SEM analysis of the failed regions after 500 h of cyclic testing in Fig. 15 provides further insight into the degradation mechanism. The failure is characterized by localized macro-grooves that penetrate the PEO layer, extending into the substrate in a pitting-like morphology. This confirms that the aggressiveness of the cyclic wet/dry test induces a localized breakdown of the oxide barrier, likely initiated at coating defects where salt crystallization during dry phases leads to extreme local chloride concentrations. Cross-sectional imaging reveals that the degradation mechanism is fundamentally identical across all coating formulations (Fig. 15). The failure triggers a localized chemical and mechanical breakdown that overcomes the barrier

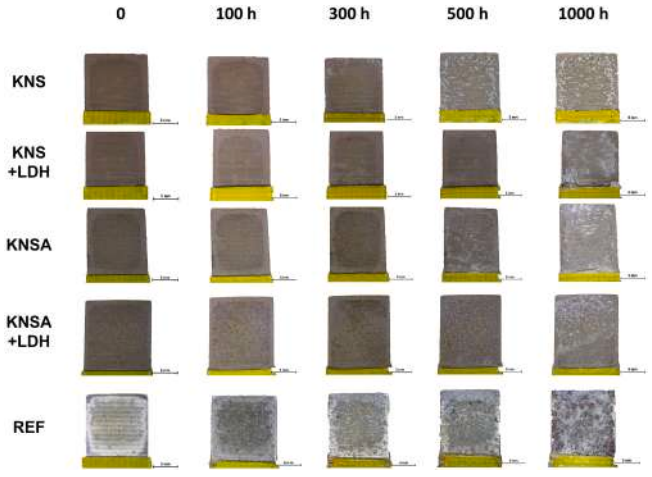

Fig. 12. Optical appearance of textured PEO-coated AA2024 samples during 1000 h of dilute electrolyte cyclic fog/dry test (ASTM G85). The images show the progressive formation of white corrosion products and localized degradation sites across all coating formulations (KNS, KNS+LDH, KNSA, KNSA+LDH) and the reference alloy (REF).

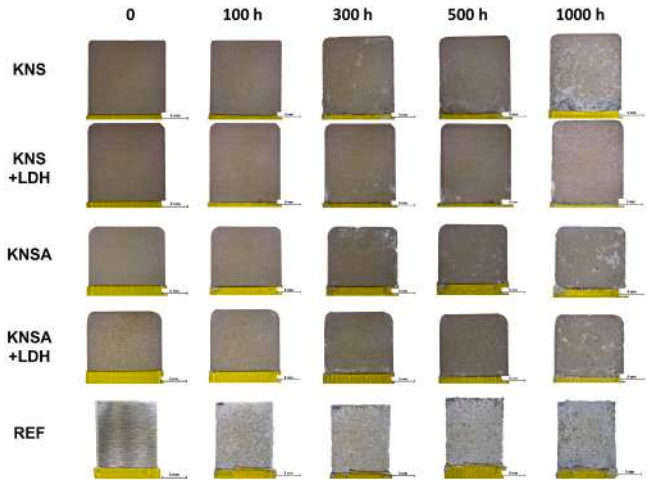

Fig. 13. Optical appearance of flat PEO-coated AA2024 samples during 1000 h of dilute electrolyte cyclic fog/dry test (ASTM G85). The figure illustrates the higher aggressiveness of the cyclic wet/dry conditions compared to the continuous salt spray test, leading to visible surface failures after 300/500 h.

properties of the hybrid systems regardless of the initial oxide compactness or sealing treatment. Under these specific conditions, the severity of the localized attack at coating defects masks the performance differences observed in less aggressive environments, leading to comparable structural damage for both the unsealed reference and the optimized PEO system.

Overall, the optimized PEO systems confirmed their strong resistance to environmental stresses. The oxidation induces color variations and limited surface early defectiveness observed on the textured coatings. The discrepancy of performances between the accelerated tests highlights a critical limitation in standard qualification protocols: reliance solely on continuous NSST may significantly overestimate the service life of porous PEO coatings, as it fails to capture the accelerated degradation driven by salt crystallization and local chloride concentration typical of realistic atmospheric weathering.

4. Discussion

The overall results indicate that the corrosion performance of PEO coatings on AA2024 substrates is governed by a delicate interplay between electrolyte composition, plasma discharge characteristics, and subsequent post-treatment. The systematic variation of hydroxide content [11], acetic acid addition, and sealing allowed the identification of key mechanisms controlling oxide growth, microstructural integrity, and long-term durability. In the acetic-acid-modified electrolyte (KNSA), the presence of acetate ions (CH_3COO^-), generated under alkaline conditions, alters the interfacial processes occurring during PEO. The addition of acetic acid to the silicate-based electrolyte serves a twofold purpose: primarily for acidification and pH control, typically reaching a stable range of 3.1–3.3 [41], and secondarily as a discharge modulator. While direct quantitative studies on isolated acetic acid effects are scarce in general PEO literature, it is established that changes in electrolyte chemistry and ionic content strongly alter discharge regimes and phase distribution [42,43]. By analogy with other additives such as Na_2WO_4 or K_2ZrF_6, which promote smoother surfaces and reduced discharge hole density [44,45], acetate species may adsorb at active sites of the growing oxide and influence the local electric field distribution across the dielectric layer. This effect can moderate the intensity of individual plasma discharges, favoring a higher density of lower-energy micro-discharges instead of fewer high-energy events. As a consequence, coating growth becomes more uniform and less affected by deep discharge channels, resulting in reduced through-thickness porosity and improved compactness. Furthermore, possible transient complexation of

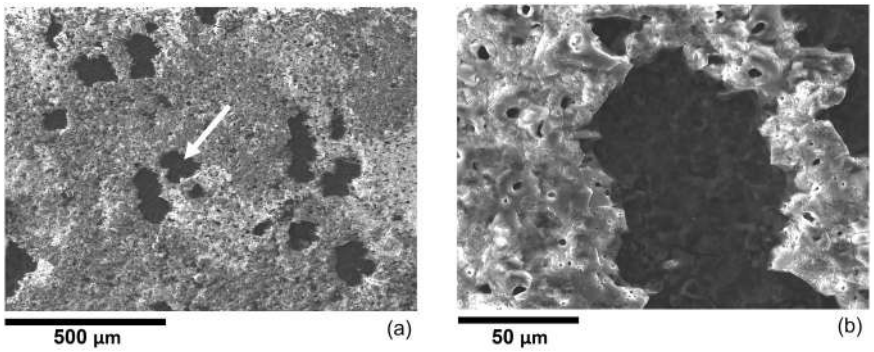

Fig. 14. Scanning Electron Microscopy (SEM) analysis of the failure morphologies after the cyclic fog/dry test. (a) Low-magnification view showing the formation of crater-like defects and localized pits (white arrow); (b) High-magnification detail of a degraded area showing the breakdown of the oxide barrier layer and the accumulation of corrosion products.

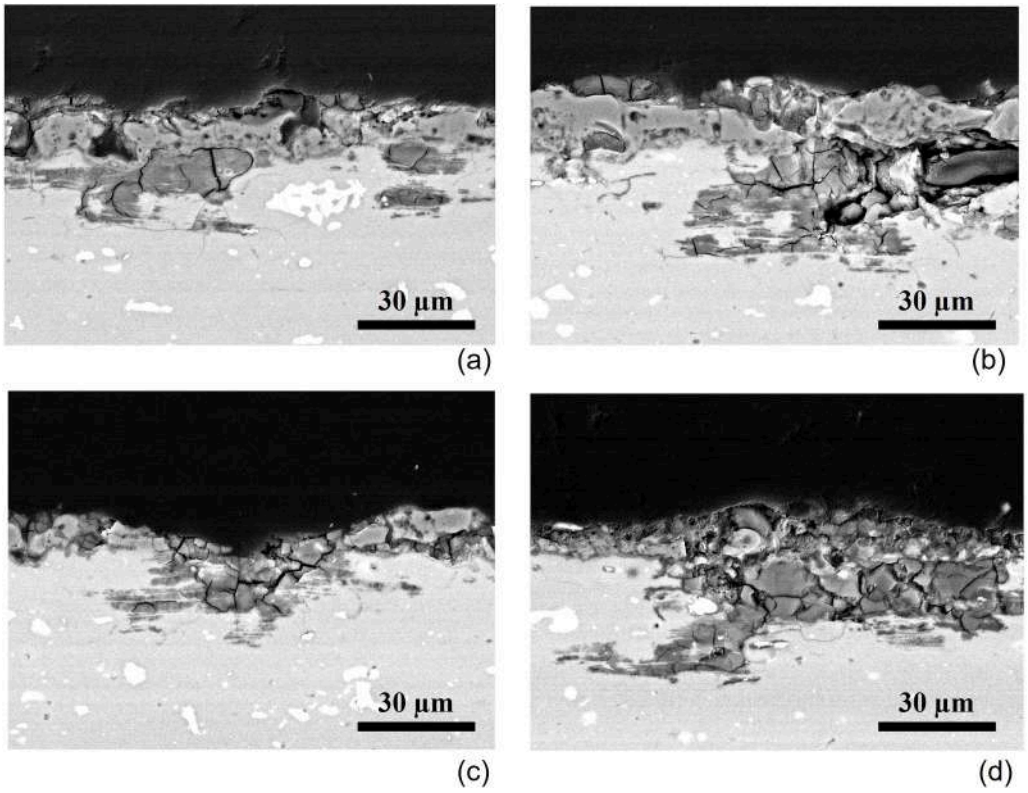

Fig. 15. SEM cross-sections of (a) KNS, (b) KNS+LDH, (c) KNSA, and (d) KNSA+LDH samples after 500 h of cyclic Prohesion testing. The micrographs illustrate an identical failure mechanism characterized by localized grooves perforating the oxide layer and penetrating deep into the AA2024 substrate.

Al^{3+} ions in the near-interface region may regulate their outward migration, contributing to controlled oxide thickening and influencing the final coating morphology. This behavior aligns with the findings of Gamba *et al.* [31] and Rogov and Shayapov [46], who observed that organic additives in PEO baths stabilize the oxide-electrolyte interface and mitigate dielectric breakdown. In this study, acetic acid effectively acted as a soft template, favoring controlled oxide growth and decreasing the tendency toward localized overheating and gas evolution, which are known to generate through-thickness porosity in traditional silicate-hydroxide systems. Although direct plasma diagnostics (e.g., high-speed imaging or optical emission spectroscopy) were not performed in the present study, several indirect experimental observations consistently indicate that the addition of acetic acid modifies the discharge regime during PEO processing. Under identical electrical parameters, the acetic-acid-modified electrolyte produced coatings with significantly reduced thickness (14 ± 1 µm) compared to the standard silicate electrolyte (19 ± 1 µm). This thickness reduction, coupled with improved corrosion resistance, suggests a change in discharge energy density rather than a simple decrease in oxide growth rate. If coating formation were governed solely by reduced oxidation kinetics, a proportional deterioration in electrochemical performance would be expected, which is not observed. Morphological analysis further supports this interpretation. SEM observations reveal that KNSA coatings exhibit a finer pore distribution, reduced microcrack density, and a more homogeneous compact inner layer compared to KNS. Such features are typically associated with moderated micro-discharges and lower local thermal stresses during plasma events. As discussed, from a physicochemical standpoint, in the strongly alkaline electrolyte used for PEO, the adsorption of acetate species at active breakdown sites may locally alter interfacial conductivity and dielectric properties of the growing oxide, thereby influencing breakdown probability and discharge intensity. While this mechanism is consistent with previous literature

reports on organic electrolyte additives [15,46], the present work demonstrates its macroscopic consequences through measurable changes in coating structure and electrochemical behaviour. The discharge-modulating effect becomes particularly relevant on riblet-textured substrates produced via TMEMM, where curvature-induced electric field gradients typically promote localized high-energy discharges at riblet crests. The improved uniformity observed for KNSA coatings on textured specimens suggests that electrolyte modification contributes to mitigating discharge localization effects associated with surface geometry.

The post-treatment, based on the hydrothermal conversion of the outer alumina layer into ZnAl-LDH, provided a second level of protection. The LDH lamellae, formed through partial ion exchange between Al^{3+} and Zn^{2+} in the near-surface region, generated a composite barrier layer with improved ionic resistivity. This layered structure hinders both chloride ingress and oxygen diffusion, as evidenced by the decrease in oxygen reduction current density and the significant increase in polarization resistance observed in EIS measurements [21]. The beneficial effect of sealing was most pronounced on the KNS coating, whose initial oxide layer exhibited higher defectiveness. In this case, the availability of Al^{3+} ions released during the hydrothermal treatment favored extensive LDH formation, producing a dense, adherent sealing layer. Conversely, for the KNSA coating, whose oxide was already compact, the sealing treatment further enhanced corrosion resistance, but to a lesser extent, suggesting a saturation effect in the hydrothermal conversion process.

The presence of ZnAl–LDH after hydrothermal treatment was confirmed by SEM morphology and EDS elemental mapping, which revealed lamellar features enriched in Zn and Al species partially filling surface-connected pores. While the present study does not provide direct quantitative measurements of pore filling percentage or adhesion strength, the electrochemical response offers indirect evidence of effective sealing. Compared to unsealed PEO coatings, LDH-treated specimens exhibit a consistent increase in polarization resistance and low-frequency impedance modulus in both dilute (20 ppm Cl^-) and concentrated (20,000 ppm Cl^-) chloride environments. The improvement is observed despite negligible changes in total coating thickness, indicating that the protective enhancement arises primarily from pore occlusion and barrier refinement rather than additional oxide growth. The duration of 15 min was selected based on preliminary process optimization. Shorter treatments resulted in incomplete lamellar development within pores, whereas longer exposure did not produce further electrochemical improvement and instead led to superficial agglomeration of LDH crystallites. Therefore, 15 min represents a practical balance between in-pore growth and surface overaccumulation under the adopted conditions.

The synergistic effect between the refined oxide structure (due to acetic acid) and the LDH top layer resulted in the superior performance of the KNSA + LDH system, which consistently achieved the highest impedance values and lowest current ranges. This synergy supports the concept of a hybrid barrier system, where the PEO oxide provides the primary physical barrier while the LDH phase supplies self-sealing capability through anion-exchange and pH-buffering mechanisms [12, 20].

A notable finding of this study is the influence of surface topography on PEO coating formation and corrosion behavior. The geometric parameters of the biomimetic texture used in this study were selected based on our previous research [17], which specifically addressed the influence of TMEMM process parameters on the resulting riblet morphology and its tolerance limits. Building upon those results, this investigation evaluates the feasibility of functionalizing such optimized surfaces with a topography-following PEO coating, shifting the focus toward the long-term environmental durability of the integrated system. The biomimetic riblet texture introduces local variations in electric field intensity during anodization. Sharp crests and deep grooves act as preferential sites for discharge initiation, resulting in uneven plasma activity and non-uniform oxide growth. SEM observations and electrochemical data revealed that coatings on textured substrates exhibited higher porosity and reduced impedance compared to those on flat ones, even when identical process parameters were applied.

The reduced performance of textured coatings is not attributed to thickness variations, as comparable average values were observed, but rather to localized microstructural discontinuities and increased through-pore connectivity. These defects promote electrolyte ingress during immersion and accelerate localized corrosion, particularly under cyclic humidity conditions. However, the application of LDH sealing substantially mitigated this issue, restoring a significant portion of the lost impedance and confirming the sealing layer's capacity to homogenize the surface response. Furthermore, the geometrical features were well preserved during the early stages of degradation, ensuring that functionality remained intact.

The observed degradation mechanisms in cyclic humidity can be interpreted as a direct consequence of the coupling between macroscopic surface topography and microscopic oxide growth. While flat substrates benefit from a uniform electric field that promotes consistent dielectric breakdown and densification, textured surfaces are subject to curvature-induced field gradients. These gradients intensify discharge activity at the ridge tips and reduce it within the valleys. This asymmetry results in localized variations in coating porosity, creating preferential pathways for ionic transport. The addition of acetic acid mitigates these geometric effects by limiting the discharge energy.

Importantly, the degradation observed in textured samples remained superficial and non-catastrophic. Even after 2000 h of salt spray, no substrate attack or coating delamination occurred. This suggests that while the texturing process introduces local challenges for oxide uniformity, the overall system retains adequate durability for functional applications requiring aerodynamic or hydrodynamic surface modification. To further assess the engineering significance of the proposed treatments, a comparison with literature data for high-performance protection systems on AA2024 is presented. Conventional chromate-free industrial treatments, such as tartaric-sulfuric acid or boric-sulfuric acid anodizing, can provide NSST reaching up to 2000 h, depending strictly on the quality and type of the sealing step [47–49]. In the present study, the potential-controlled PEO layer coupled with LDH sealing matched these high-end industrial benchmarks, showing minimal degradation after 2000 h of exposure. It is important to emphasize that this level of protection was achieved not only on flat surfaces but also on biomimetically textured substrates. The preservation of such high durability on complex riblet geometries is noteworthy, as surface protrusions and cavities typically act as preferential sites for coating defects and localized corrosive attack. Regarding the Prohesion test, a direct comparison remains challenging due to the scarcity of published benchmarks for AA2024, which underscores the importance of the data presented in this study.

Furthermore, from a design standpoint, these findings confirm that optimized PEO and LDH treatments offer a robust compromise between corrosion resistance and surface functionality, preserving the drag-reducing riblet morphology while ensuring extended electrochemical stability. Looking forward, overcoming the residual geometric constraints of textured surfaces requires shifting from empirical process tuning to a predictive 'design-for-coating' approach. Future investigations should therefore focus on quantifying the relationship between curvature-induced field enhancement and localized discharge intensification, which serves as the primary driver for the increased defect density observed at riblet crests. This insight will be crucial for guiding the optimization of riblet aspect ratios to ensure uniform oxide growth without compromising aerodynamic efficiency. Ultimately, such a transition toward geometry-aware processing will be essential to successfully combine advanced fluid-dynamic features with long-term environmental durability in realistic operational environments.

5. Conclusions

This investigation provides a comprehensive validation of potential-controlled Plasma Electrolytic Oxidation (PEO) and ZnAl-Layered Double Hydroxide (LDH) sealing as a robust strategy for the environmental protection of biomimetically textured AA2024 alloys. Despite the inherent challenges posed by the microstructural heterogeneity of the AA2024 alloy, specifically the presence of Cu-rich intermetallic particles that promote localized electrochemical instability, the optimized PEO process successfully produced homogeneous and highly adherent oxide layers on complex riblet geometries. A fundamental achievement of this work is the strict preservation of the functional riblet profile, where the PEO coating demonstrated exceptional morphological fidelity by maintaining the designed pitch and depth without compromising the sharp crests essential for aerodynamic efficiency. Electrochemical characterization revealed that while the anti-corrosion properties of the textured surfaces are comparable to those of flat substrates, the corrugated geometry induces a localized increase in porosity that slightly reduces overall stability. The critical role of 10 g/L acetic acid in regulating plasma discharge kinetics was demonstrated by the growth of a denser barrier layer; specifically, the sealed KNS+LDH system on textured riblets achieved a low-frequency impedance modulus ($Z_{0.01\ Hz}$) of $1.7{\cdot}10^{6}$ Ω·cm² in freshwater, compared to $2.9{\cdot}10^{7}$ Ω·cm² for its flat counterpart. In aggressive simulated seawater, the acetic-acid-modified KNSA+LDH system on textured substrates maintained a stable impedance of $5.0{\cdot}10^{5}$ Ω·cm², significantly outperforming the bare alloy (10^{3} Ω·cm²). The comparative assessment of accelerated aging tests underscored that environmental conditions profoundly influence the durability of these protective systems. While the hybrid PEO-LDH coatings matched high-end industrial chromate-free benchmarks by sustaining 2000 h of continuous neutral salt spray exposure with no evidence of sub-surface corrosion, a markedly different behaviour was observed under cyclic wet/dry Prohesion testing. In the latter case, localized degradation appeared after approximately 500 h, driven by the cyclic crystallization of salts that promotes extreme local concentrations of aggressive ions, eventually triggering a localized perforation of the oxide barrier. Furthermore, the optimized hydrothermal treatment provided significant surface ennoblement but achieved only partial sealing of the innermost pore network on the riblet crests. Moving forward, the research outlook will prioritize the aerodynamic validation of these durable coatings in wind tunnel facilities to quantify the actual drag reduction efficiency under realistic operational environments, confirming the feasibility of integrating advanced fluid-dynamic features with robust environmental durability for sustainable aeronautical components.

CRediT authorship contribution statement

Andrea Cristoforetti: Writing – review & editing, Writing – original draft, Methodology, Investigation, Data curation, Conceptualization. **Marco Ormellese:** Supervision, Resources, Project administration, Funding acquisition. **Michele Fedel:** Writing – review & editing, Validation, Supervision, Resources, Project administration, Funding acquisition. **Matteo Gamba:** Writing – review & editing, Investigation, Data curation, Conceptualization. **Andrea Brenna:** Writing – review & editing, Validation, Supervision, Resources, Project administration, Methodology, Funding acquisition.

Declaration of Competing Interest

The authors declare the following financial interests/personal relationships which may be considered as potential competing interests: Andrea Cristoforetti reports financial support was provided by Ministero dell'Università e della Ricerca. If there are other authors, they declare that they have no known competing financial interests or personal relationships that could have appeared to influence the work reported in this paper.

Acknowledgments

The authors acknowledge funding by EUROPEAN UNION – NEXT GENERATION EU, PNRR - MISSIONE 4 "ISTRUZIONE E RICERCA" - COMPONENTE C2 INVESTIMENTO 1.1 "FONDO PER IL PROGRAMMA NAZIONALE DI RICERCA E PROGETTI DI RILEVANTE INTERESSE NAZIONALE (PRIN)" D.D. N. 104/2022 "BANDO PRIN 2022". PE11 Engineering of Metals and alloys.

Appendix

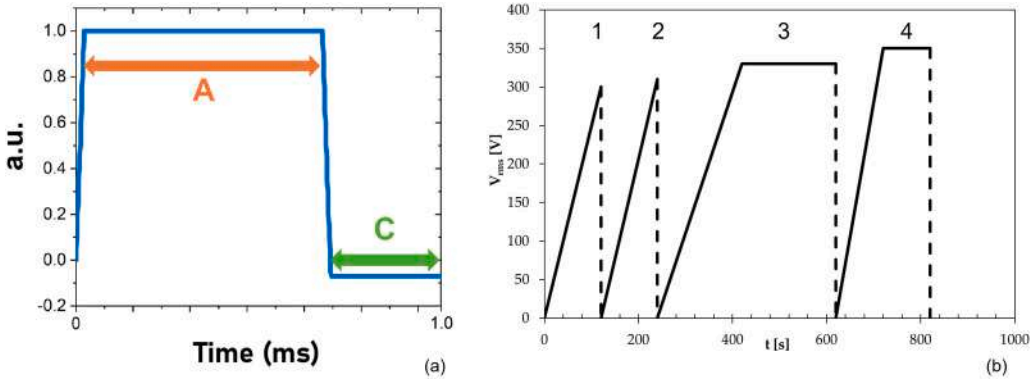

Fig. A.1. (a) reports the square wave used for PEO anodizing of AA2024 specimens. Letter A stands for anodic polarization time (60% of the period), letter C for cathodic polarization time (40% of the period); vertical axis is in arbitrary units. In (b) the evolution of the root-mean-square voltage applied to the specimen during PEO anodizing. The procedure is divided in 4 steps with different voltages and polarization periods

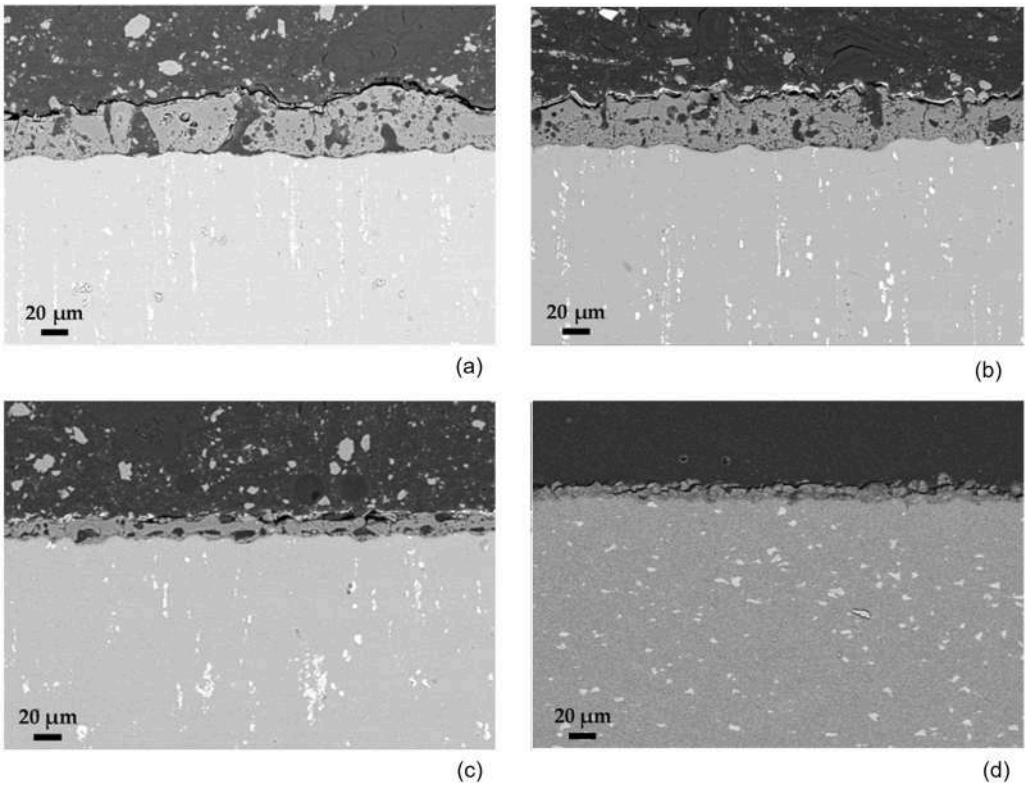

Fig. A.2. Scanning Electron Microscopy (SEM) micrographs showing the cross-sectional morphology of Plasma Electrolytic Oxidation (PEO) coatings applied to flat aluminium alloy AA2024 substrates: (a) reference silicate-based coating (KNS); (b) reference coating sealed with ZnAl Layered Double Hydroxides (KNS+LDH); (c) coating produced in an electrolyte modified with acetic acid (KNSA); (d) acetic-acid-modified coating sealed with Layered Double Hydroxides (KNSA+LDH). The scale bars represent 20 µm

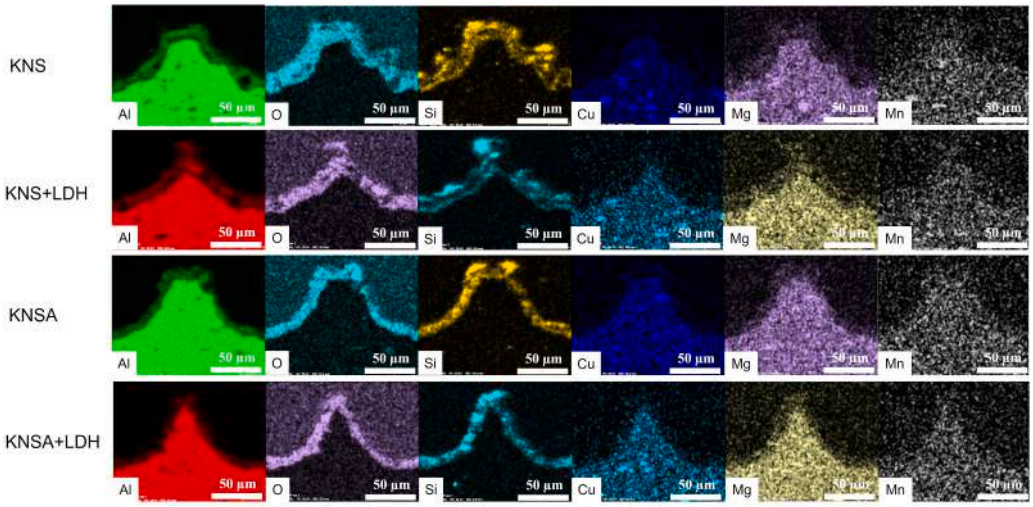

Fig. A.3. SEM-EDS maps of the three coatings in cross-section for their main elemental constituents (Al, O, Si, Cu, Mg and Mn)

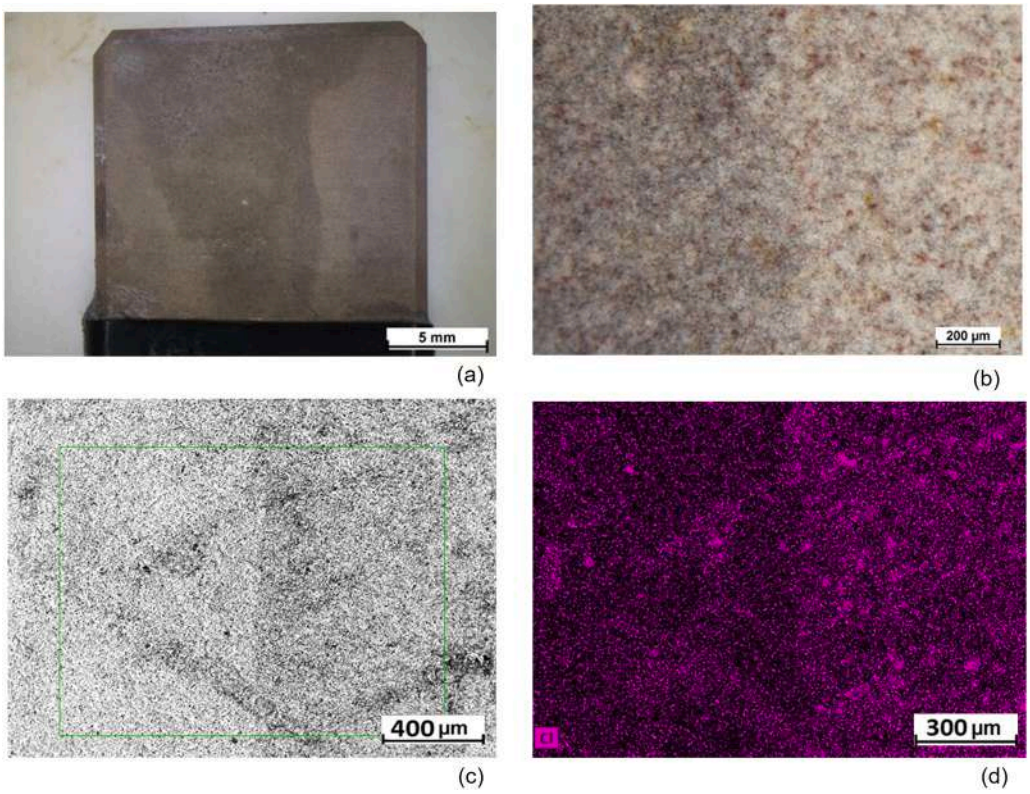

Fig. A.4. Comprehensive investigation of the localized surface darkening phenomenon observed on the Plasma Electrolytic Oxidation (PEO) coating after 2000 h of exposure to the Neutral Salt Spray Test (NSST). (a) Macroscopic optical image of the AA2024 sample highlighting the discoloured area; (b) high-magnification optical micrograph focusing on the transition zone between the darkened and original coating surface; (c) Scanning Electron Microscopy (SEM) micrograph of the analysed region; (d) corresponding Energy Dispersive X-ray Spectroscopy (EDXS) elemental map of Chlorine (Cl). The localized presence of Chlorine in the darkened areas, in the absence of substrate pits or voluminous corrosion products, suggests a superficial adsorption and trapping phenomenon. This observation confirms that the chromatic variation is likely due to a superficial interaction and localized surface modification rather than a localized corrosive failure of the barrier

Data Availability

Data will be made available on request.

References

[1] J. DeRose, A. Bałkowiec, J. Michalski, T. Suter, K. Kurzydlowski, P. Schmutz, Microscopic and macroscopic characterisation of an aerospace aluminium alloy (AA2024), Witpress (2012).
[2] A. Boag, A.E. Hughes, A.M. Glenn, T.H. Muster, D. McCulloch, Corrosion of AA2024-T3 Part I: localised corrosion of isolated IM particles, Corros. Sci. 53 (2011) 17–26, https://doi.org/10.1016/j.corsci.2010.09.009.
[3] A. Cristoforetti, M. Gamba, A. Brenna, M. Ormellese, M. Fedel, Influence of intermetallics on through-mask electrochemical micromachining for surface texturing of aluminum alloys, Surf. Coat. Technol. (2025) 132273, https://doi.org/10.1016/j.surfcoat.2025.132273.
[4] N. Birbilis, R.G. Buchheit, Electrochemical characteristics of intermetallic phases in aluminum alloys: an experimental survey and discussion, J. Electrochem. Soc. 152 (2005) B140.
[5] M. Olgiati, P.J. Denissen, S.J. Garcia, When all intermetallics dealloy in AA2024-T3: quantifying early stage intermetallic corrosion kinetics under immersion, Corros. Sci. 192 (2021) 109836, https://doi.org/10.1016/j.corsci.2021.109836.
[6] G.E. Thompson, Porous anodic alumina: fabrication, characterization and applications, Thin Solid Films 297 (1997) 192–201, https://doi.org/10.1016/S0040-6090(96)09440-0.
[7] R.L. Twite, G.P. Bierwagen, Review of alternatives to chromate for corrosion protection of aluminum aerospace alloys, Prog. Org. Coat. 33 (1998) 91–100, https://doi.org/10.1016/S0300-9440(98)00015-0.
[8] K.A. Yasakau, M.L. Zheludkevich, O.V. Karavai, M.G.S. Ferreira, Influence of inhibitor addition on the corrosion protection performance of sol–gel coatings on AA2024, Prog. Org. Coat. 63 (2008) 352–361, https://doi.org/10.1016/j.porgcoat.2007.12.002.
[9] B. Syrek-Gerstenkorn, S. Paul, A.J. Davenport, Sacrificial thermally sprayed aluminium coatings for marine environments: a review, Coatings 10 (2020) 267, https://doi.org/10.3390/coatings10030267.
[10] P. Deng, W. Mo, Z. Ouyang, K. Ling, B. Luo, Z. Bai, Microstructural evolution and corrosion mechanism of micro-alloyed 2024 (Zr, Sc, Ag) aluminum alloys, Corros. Sci. 224 (2023) 111476, https://doi.org/10.1016/j.corsci.2023.111476.
[11] M. Gamba, A. Cristoforetti, M. Fedel, F. Ceriani, M. Ormellese, A. Brenna, Plasma Electrolytic Oxidation (PEO) coatings on aluminum alloy 2024: a review of mechanisms, processes, and corrosion resistance enhancement, Appl. Surf. Sci. Adv. 26 (2025) 100707, https://doi.org/10.1016/j.apsadv.2025.100707.
[12] F. Peng, D. Wang, Y. Tian, H. Cao, Y. Qiao, X. Liu, Sealing the pores of PEO coating with Mg-Al layered double hydroxide: enhanced corrosion resistance, cytocompatibility and drug delivery ability, Sci. Rep. 7 (2017) 8167, https://doi.org/10.1038/s41598-017-08238-w.
[13] L. Sopchenski, J. Robert, M. Touzin, A. Tricoteaux, M.-G. Olivier, Improvement of wear and corrosion protection of PEO on AA2024 via sol-gel sealing, Surf. Coat. Technol. 417 (2021) 127195, https://doi.org/10.1016/j.surfcoat.2021.127195.
[14] F. Ceriani, L. Casanova, M. Ormellese, Use of organic acids as additives for plasma electrolytic oxidation (PEO) of titanium, Coatings 14 (2024) 703, https://doi.org/10.3390/coatings14060703.
[15] L. Casanova, F. Ceriani, M. Pedeferri, M. Ormellese, Addition of organic acids during PEO of titanium in alkaline solution, Coatings 12 (2022) 143, https://doi.org/10.3390/coatings12020143.
[16] Y. Li, S. Yang, Y. Wan, Enhancing the corrosion resistance of plasma electrolytic oxidation coatings by plasticizing chitosan films with glycerol, Ceram. Int. 51 (2025) 30394–30404, https://doi.org/10.1016/j.ceramint.2025.04.233.
[17] A. Cristoforetti, M. Gamba, A. Brenna, M. Ormellese, M. Fedel, Advancing aeronautical surface texturing: through-mask electrochemical micromachining of aluminum AA2024-T3 for drag reduction applications, Surf. Coat. Technol. 504 (2025) 132061, https://doi.org/10.1016/j.surfcoat.2025.132061.
[18] T. Baldhoff, V. Nock, A. Marshall, Through-mask electrochemical micromachining, J. Electrochem. Soc. 165 (2018) E841.
[19] Y. Sun, S. Ling, D. Zhao, J. Liu, Z. Liu, J. Song, Through-mask electrochemical micromachining of micro pillar arrays on aluminum, Surf. Coat. Technol. 401 (2020) 126277, https://doi.org/10.1016/j.surfcoat.2020.126277.
[20] M. Mohedano, M. Serdechnova, M. Starykevich, S. Karpushenkov, A.C. Bouali, M. G.S. Ferreira, M.L. Zheludkevich, Active protective PEO coatings on AA2024: role of voltage on in-situ LDH growth, Mater. & Des. 120 (2017) 36–46, https://doi.org/10.1016/j.matdes.2017.01.097.
[21] G. Liu, X. Lu, X. Zhang, T. Zhang, F. Wang, Improvement of corrosion resistance of PEO coatings on Al alloy by formation of ZnAl layered double hydroxide, Surf.

Coat. Technol. 441 (2022) 128528, https://doi.org/10.1016/j.surfcoat.2022.128528.
[22] A.C. Bouali, M. Serdechnova, C. Blawert, J. Tedim, M.G.S. Ferreira, M. L. Zheludkevich, Layered double hydroxides (LDHs) as functional materials for the corrosion protection of aluminum alloys: a review, Appl. Mater. Today 21 (2020) 100857, https://doi.org/10.1016/j.apmt.2020.100857.
[23] M. Serdechnova, M. Mohedano, B. Kuznetsov, C.L. Mendis, M. Starykevich, S. Karpushenkov, J. Tedim, M.G.S. Ferreira, C. Blawert, M.L. Zheludkevich, PEO coatings with active protection based on in-situ formed LDH-nanocontainers, J. Electrochem. Soc. 164 (2016) C36, https://doi.org/10.1149/2.0301702jes.
[24] A.C. Bouali, E.A. Straumal, M. Serdechnova, D.C.F. Wieland, M. Starykevich, C. Blawert, J.U. Hammel, S.A. Lermontov, M.G.S. Ferreira, M.L. Zheludkevich, Layered double hydroxide based active corrosion protective sealing of plasma electrolytic oxidation/sol-gel composite coating on AA2024, Appl. Surf. Sci. 494 (2019) 829–840, https://doi.org/10.1016/j.apsusc.2019.07.117.
[25] M. Serdechnova, M. Mohedano, A.C. Bouali, D. Höche, B. Kuznetsov, S. Karpushenkov, C. Blawert, M.L. Zheludkevich, Role of phase composition of PEO Coatings on AA2024 for In-Situ LDH growth, Coatings 7 (2017) 190, https://doi.org/10.3390/coatings7110190.
[26] M.A. Iqbal, H. Asghar, E. Matykina, R. Arrabal, M. Mohedano, J.M. Vega, Synergy of consecutive PEO and LDH surface treatments on the corrosion protection and adhesion strength of organic coatings on AA2024T3, Prog. Org. Coat. 207 (2025) 109397, https://doi.org/10.1016/j.porgcoat.2025.109397.
[27] ASTM B117-19, Standard Practice for Operating Salt Spray (Fog) Apparatus, (2019). https://doi.org/10.1520/B0117-19.
[28] ASTM G85-19, Standard Practice for Modified Salt Spray (Fog) Testing, (2019). https://doi.org/10.1520/G0085-19.
[29] F. Ceriani, L. Casanova, L. Massimini, A. Brenna, M. Ormellese, TiO2 microparticles incorporation in coatings produced by plasma electrolytic oxidation (PEO) on titanium, Coatings 13 (2023) 1718, https://doi.org/10.3390/coatings13101718.
[30] L. Casanova, M. Arosio, M.T. Hashemi, M. Pedeferri, G. Botton, M. Ormellese, Influence of stoichiometry on the corrosion response of titanium oxide coatings produced by plasma electrolytic oxidation, Corros. Sci. 203 (2022) 110361.
[31] M. Gamba, A. Cristoforetti, M. Fedel, F. Ceriani, M. Ormellese, A. Brenna, Potential-controlled PEO coatings on biomimetic textured AA2024: treatment optimization and corrosion resistance, Electrochim. Acta (2025) 147409, https://doi.org/10.1016/j.electacta.2025.147409.
[32] M. Javidi, H. Fadaee, Plasma electrolytic oxidation of 2024-T3 aluminum alloy and investigation on microstructure and wear behavior, Appl. Surf. Sci. 286 (2013) 212–219, https://doi.org/10.1016/j.apsusc.2013.09.049.
[33] H. Fadaee, M. Javidi, Investigation on the corrosion behaviour and microstructure of 2024-T3 Al alloy treated via plasma electrolytic oxidation, J. Alloy. Compd. 604 (2014) 36–42, https://doi.org/10.1016/j.jallcom.2014.03.127.
[34] F. Ceriani, P. Shashkov, S. Usov, M. Ormellese, M. Pedeferri, Sealing post-treatments of coatings produced by electrochemical oxidation (ECO) on aluminum AA2024, Meet. Abstr. MA2025-02 (2025) 1139, https://doi.org/10.1149/MA2025-02131139mtgabs.
[35] K. Du, X. Guo, Q. Guo, Y. Wang, F. Wang, Y. Tian, Effect of PEO coating microstructure on corrosion of Al 2024, J. Electrochem. Soc. 159 (2012) C597, https://doi.org/10.1149/2.005301jes.
[36] G. Zhang, E. Jiang, L. Wu, W. Ma, H. Yang, A. Tang, F. Pan, Corrosion protection properties of different inhibitors containing PEO/LDHs composite coating on magnesium alloy AZ31, Sci. Rep. 11 (2021) 2774, https://doi.org/10.1038/s41598-021-81029-6.
[37] S. Javadi, L. Castro, R. Arrabal, E. Matykina, S. Javadi, L. Castro, R. Arrabal, E. Matykina, Metal ion release from PEO-Coated Ti6Al4V DMLS alloy for orthopedic implants, J. Funct. Biomater. 16 (2025), https://doi.org/10.3390/jfb16100362.
[38] R.G. Buchheit, S.B. Mamidipally, P. Schmutz, H. Guan, Active corrosion protection in Ce-modified hydrotalcite conversion coatings, Corrosion 58 (2002) 3–14, https://doi.org/10.5006/1.3277303.
[39] M.L. Zheludkevich, S.K. Poznyak, L.M. Rodrigues, D. Raps, T. Hack, L.F. Dick, T. Nunes, M.G.S. Ferreira, Active protection coatings with layered double hydroxide nanocontainers of corrosion inhibitor, Corros. Sci. 52 (2010) 602–611, https://doi.org/10.1016/j.corsci.2009.10.020.
[40] T. Arunnellaiappan, L. Rama Krishna, S. Anoop, R. Uma Rani, N. Rameshbabu, Fabrication of multifunctional black PEO coatings on AA7075 for spacecraft applications, Surf. Coat. Technol. 307 (2016) 735–746, https://doi.org/10.1016/j.surfcoat.2016.09.043.
[41] Z. Peng, H. Xu, S. Liu, Y. Qi, J. Liang, Wear and corrosion resistance of plasma electrolytic oxidation coatings on 6061 Al alloy in electrolytes with aluminate and phosphate, Materials 14 (2021) 4037, https://doi.org/10.3390/ma14144037.
[42] A.G. McCarroll, P.L. Menezes, Modern innovations and applications in plasma electrolytic oxidation coatings on aluminum, magnesium, and titanium, Coatings 15 (2025) 592, https://doi.org/10.3390/coatings15050592.
[43] X. Li, Plasma electrolytic oxidation process for corrosion protection of two aluminium alloys used in automotive applications., (2006). ⟨https://hdl.handle.net/20.500.14776/2761⟩ (accessed February 23, 2026).
[44] S.B. Orgen, E.M.B. Dela Peña, Microstructure, hardness, and corrosion behavior of oxidized AA6061 using potentiostatic plasma electrolytic oxidation, Coatings 15 (2025) 1129, https://doi.org/10.3390/coatings15101129.
[45] D.V. Dzhurinskiy, S.S. Dautov, P.G. Shornikov, I.S. Akhatov, Surface modification of aluminum 6061-O alloy by plasma electrolytic oxidation to improve corrosion resistance properties, Coatings 11 (2021) 4, https://doi.org/10.3390/coatings11010004.
[46] A.B. Rogov, V.R. Shayapov, The role of cathodic current in PEO of aluminum: Influence of cationic electrolyte composition on the transient current-voltage curves and the discharges optical emission spectra, Appl. Surf. Sci. 394 (2017) 323–332, https://doi.org/10.1016/j.apsusc.2016.10.115.
[47] G. Ouaziz, O. Savadogo, The cathodic breakdown test to assess chromic acid anodized aluminum alloys corrosion protection performance, in correlation with salt spray (Fog) testing, Int. Sch. Res. Not. 2012 (2012) 140624, https://doi.org/10.5402/2012/140624.
[48] Y. Wu, W. Zhao, W. Wang, L. Wang, Q. Xue, Novel anodic oxide film with self-sealing layer showing excellent corrosion resistance, Sci. Rep. 7 (2017) 1344, https://doi.org/10.1038/s41598-017-01549-y.
[49] M. Terada, F.M. Queiroz, D.B.S. Aguiar, V.H. Ayusso, H. Costenaro, M.-G. Olivier, H.G. de Melo, I. Costa, Corrosion resistance of tartaric-sulfuric acid anodized AA2024-T3 sealed with Ce and protected with hybrid sol–gel coating, Surf. Coat. Technol. 372 (2019) 422–426, https://doi.org/10.1016/j.surfcoat.2019.05.028.